JCB Journal of Cell Biology

ARTICLE

The α-Catenin mechanosensing M region is required for cell adhesion during tissue morphogenesis

Luka Sheppard[1], David G. Green[1], Gerald Lerchbaumer[1], Katheryn E. Rothenberg[2,3], Rodrigo Fernandez-Gonzalez[1,2,3,4], and Ulrich Tepass[1]

α-Catenin couples the cadherin–catenin complex to the actin cytoskeleton. The mechanosensitive α-Catenin M region undergoes conformational changes upon application of force to recruit interaction partners. Here, we took advantage of the tension landscape in the *Drosophila* embryo to define three different states of α-Catenin mechanosensing in support of cell adhesion. Low-, medium-, and high-tension contacts showed a corresponding recruitment of Vinculin and Ajuba, which was dependent on the α-Catenin M region. In contrast, the Afadin homolog Canoe acts in parallel to α-Catenin at bicellular low- and medium-tension junctions but requires an interaction with α-Catenin for its tension-sensitive enrichment at high-tension tricellular junctions. Individual M region domains make complex contributions to cell adhesion through their impact on interaction partner recruitment, and redundancies with the function of Canoe. Our data argue that α-Catenin and its interaction partners are part of a cooperative and partially redundant mechanoresponsive network that supports AJs remodeling during morphogenesis.

Introduction

During morphogenesis, cell contacts are subjected to contractile forces to elicit coordinated cell shape changes and cell rearrangements. Maintaining cohesion and tissue integrity during cell contact changes is believed to require the response of adherens junction (AJ) components to force. AJs are both stable enough to resist actomyosin-generated forces, yet dynamic enough to be readily disassembled and rebuilt (Lecuit and Yap, 2015; Ladoux et al., 2015; Pinheiro and Bellaïche, 2018; Charras and Yap, 2018; Clarke and Martin, 2021). The cadherin–catenin complex (CCC) at AJs physically couples the cytoskeleton of neighboring cells and in response to force—generated often by actomyosin contraction—strengthens adhesive interactions (le Duc et al., 2010; Yonemura et al., 2010). α-catenin is thought to be the central mechanosensor of the CCC (Yonemura et al., 2010; Ishiyama and Ikura, 2012; Leckband and De Rooij, 2014; Ladoux et al., 2015; Angulo-Urarte et al., 2020). Although mutational analysis of α-catenin has demonstrated its essential role for cell adhesion similar to E-cadherin (Ecad) and β-catenin (Armadillo [Arm] in *Drosophila*) in several animal species (Torres et al., 1997; Kofron et al., 1997; Costa et al., 1998; Schepis et al., 2012; Sarpal et al., 2012; Nathaniel Clarke et al., 2019) the function of α-catenin mechanosensing in tissue morphogenesis remains largely unexplored.

Transmission of cytoskeletal forces to cadherins, and the integrity of AJs, requires the physical link between cadherins and actin provided by α-catenin (Rimm et al., 1995; Desai et al., 2013; Buckley et al., 2014). Force-induced conformational changes in cadherin extra-cellular domains increases the strength of trans-interactions between cadherins of neighboring cells (Leckband and De Rooij, 2014; Pinheiro and Bellaïche, 2018). Force-induced conformational changes also occur in two mechanosensory domains of α-catenin: the central M region and the C-terminal actin-binding domain (ABD; Fig. 1, A and B). α-catenin directly binds F-actin as a catch-bond, where binding strength increases with increasing force up to a threshold. Under tension, ABD conformational changes enhance direct F-actin binding (Buckley et al., 2014; Ishiyama et al., 2018; Xu et al., 2020; Wang et al., 2022). Moreover, reversible force-induced conformational changes in the M region cause recruitment of other F-actin binding proteins, believed to reinforce adhesion (Yonemura et al., 2010; Choi et al., 2012; Rangarajan and Izard, 2012; Twiss et al., 2012; Huveneers et al., 2012; Barry et al., 2014;

[1]Department of Cell and Systems Biology, University of Toronto, Toronto, Canada; [2]Institute of Biomedical Engineering, University of Toronto, Toronto, Canada; [3]Ted Rogers Centre for Heart Research, University of Toronto, Toronto, Canada; [4]Developmental and Stem Cell Biology Program, The Hospital for Sick Children, Toronto, Canada.

Correspondence to Ulrich Tepass: u.tepass@utoronto.ca

Luka Sheppard's current affiliation is Basic Sciences Division, Fred Hutchinson Cancer Center, Seattle, WA, USA.

© 2022 Sheppard et al. This article is distributed under the terms of an Attribution–Noncommercial–Share Alike–No Mirror Sites license for the first six months after the publication date (see http://www.rupress.org/terms/). After six months it is available under a Creative Commons License (Attribution–Noncommercial–Share Alike 4.0 International license, as described at https://creativecommons.org/licenses/by-nc-sa/4.0/).

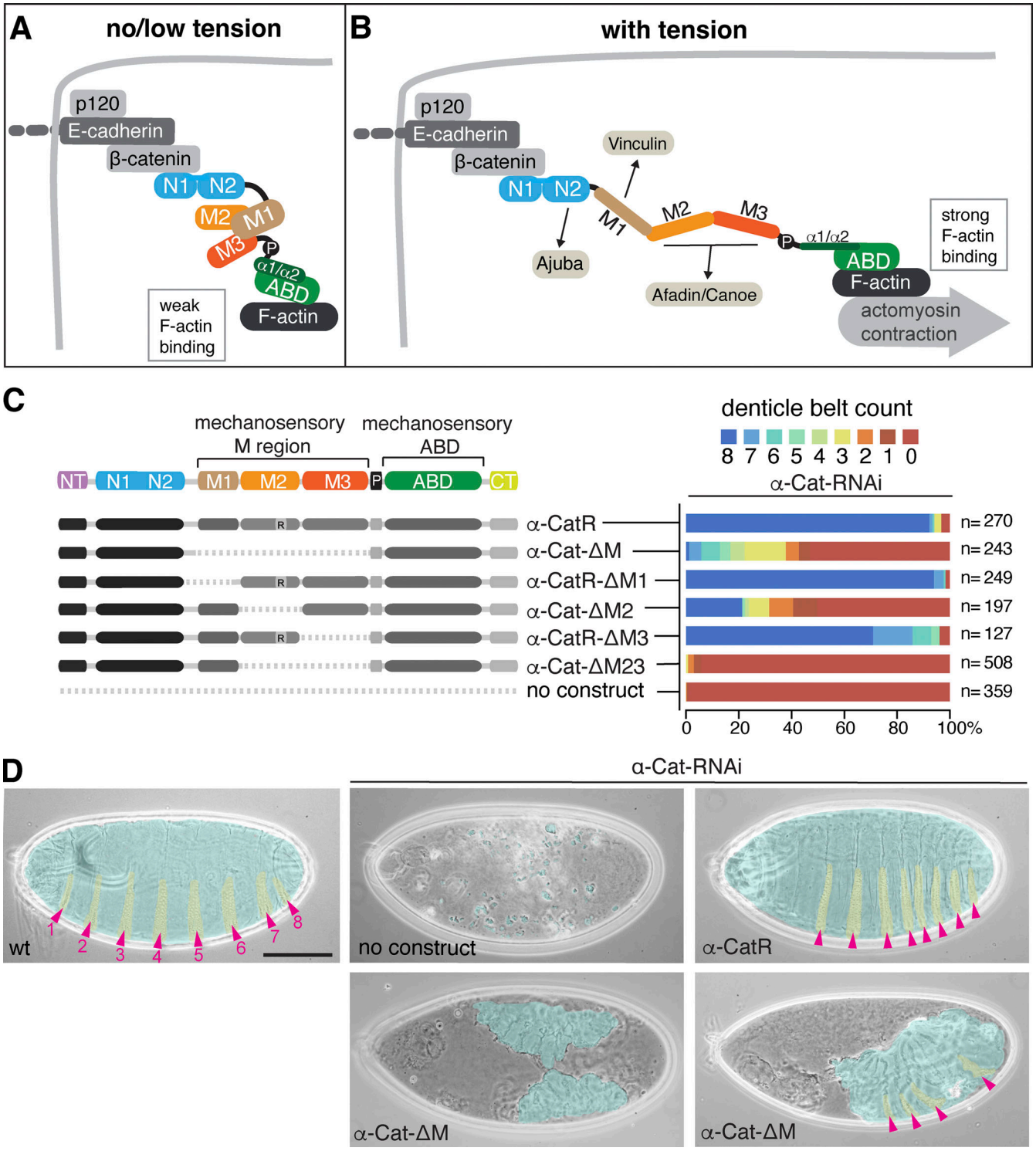

Figure 1. **The α-Cat M region is required for epithelial integrity during embryogenesis. (A and B)** Model of α-Cat under no/low and high tension, including proposed interaction partners Jub, Vinc, and Afadin/Cno that associate with α-Cat after force-induced release of autoinhibition. See text for further discussion. **(C)** Quantification of cuticle defects of embryos expressing α-CatR or α-Cat deletion constructs in an *α-Cat-RNAi* background. Number of embryos analyzed = *n*. **(D)** Representative cuticle images of embryos of the indicated genotypes. False color shading of cuticle in blue and denticle belts in yellow. Pink arrowheads point to abdominal denticle belts that were used for quantification in C. Scale bar, 100 µm. wt, wild-type.

Mège and Ishiyama, 2017; Ishiyama et al., 2018; Sarpal et al., 2019; Alégot et al., 2019).

Without tension, a dynamic electrostatic network of salt-bridges holds the α-helical bundles of M1, M2, and M3 in a closed conformation (Ishiyama et al., 2013; Li et al., 2015; Fig. 1, A and B). At forces of ~5 pN, M1 unfurls and binds Vinculin (Vinc), recruiting Vinc to the cell membrane (Yonemura et al., 2010; Ishiyama et al., 2013; Barry et al., 2014; Yao et al., 2014; Kim et al., 2015; Maki et al., 2016; Seddiki et al., 2018). Junctional recruitment of Ajuba (Jub) is also regulated by mechanosensing through the M region, with M1 limiting Jub recruitment to α-catenin (Alégot et al., 2019; Sarpal et al., 2019). At higher forces of ~10–15 pN, the M region unfolds further, partially or completely unfurling M2 and M3 (Yao et al., 2014), and the angle between M2 and M3 may increase (Ishiyama et al., 2013; Li et al., 2015). This is predicted to expose an Afadin interaction site (Pokutta et al., 2002; Ishiyama et al., 2013; Li et al., 2015; Matsuzawa et al., 2018; Sakakibara et al., 2020). A constitutively open M region α-catenin mutant increases Afadin and Vinc recruitment in cell culture (Matsuzawa et al., 2018). The α-catenin binding site on Afadin is also required for its mechanosensitive enrichment (Sakakibara et al., 2020). Hence, M region conformation states are thought to affect interaction between α-catenin and Afadin, Vinc, and Jub.

Here, we assessed the function of the M region of *Drosophila* α-Catenin (α-Cat) and its three domains (M1, M2, and M3) in embryonic morphogenesis. Contrary to expectation, α-Cat constructs lacking the entire M region can fully replace endogenous α-Cat in the wing disc epithelium (Sarpal et al., 2019). Deletion of individual M region domains also supports epithelial integrity of the wing disc and ovarian follicle (Desai et al., 2013; Sarpal et al., 2019). Partial M region deletion in zebrafish caused cell migration, but not adhesion defects, defects that were not phenocopied by *Vinc* mutants (Han et al., 2016; Han et al. 2017). Although several tissue culture studies argue that M1-dependent Vinc recruitment is essential for cadherin-based cell adhesion (Yonemura et al., 2010; le Duc et al., 2010; Huveneers et al., 2012; Twiss et al., 2012; Seddiki et al., 2018), a significant role for Vinc in AJ function is not supported by analysis of *Vinc* mutants in *Caenorhabditis elegans* (Barstead and Waterston, 1991), *Drosophila* (Alatortsev et al., 1997; Maartens et al., 2016), zebrafish (Han et al., 2017), or mouse (Xu et al., 1998). Similarly, whereas the role of M1 in limiting Jub recruitment regulates normal tissue growth (Rauskolb et al., 2014; Alégot et al., 2019; Sarpal et al., 2019), it is unclear whether this interaction supports adhesion. Jub null mutants in the mouse, zebrafish, and *Drosophila* complete embryogenesis with only subtle defects (Pratt et al., 2005; Witzel et al., 2012; Razzell et al., 2018) consistent with a minor role for Jub in cell adhesion, at best.

The only α-catenin M region interaction partner with substantive adhesion defects, though weaker than those resulting from α-catenin depletion, is Afadin (Canoe [Cno] in *Drosophila*). Loss of Cno causes mesoderm invagination defects (Sawyer et al., 2009) and tears in the ectodermal epithelium during convergent extension (Sawyer et al., 2009; Yu and Zallen, 2020). *cno* zygotic mutants have dorsal closure defects (Jürgens et al., 1984; Takahashi et al., 1998; Boettner et al., 2003; Choi et al., 2011) similar to some *α-Cat* zygotic mutants (Sarpal et al., 2012; Jurado et al., 2016). The comparatively mild-to-moderate defects produced by loss of Vinc, Jub, and Cno compared to the striking loss of epithelial integrity caused by loss of α-Cat led us to wonder (i) whether this is explained by redundancy between α-Cat interaction partners and (ii) whether, and if so how, the α-Cat M region contributes to adhesion and morphogenesis through recruitment of these interaction partners in response to force.

Vinc, Jub, and Cno show tension-sensitive distribution in the early *Drosophila* embryo, raising the possibility that their junctional recruitment is dependent on α-Cat mechanosensing. During germband extension, adhesion is challenged by rapid junction remodeling, and cell edges aligned with the dorsal–ventral (DV) axis (vertical edges) experience higher tension (Clarke and Martin, 2021; Fernandez-Gonzalez et al., 2009). Myosin becomes planar polarized, enriched at vertical edges, which contract during neighbor-exchange (Zallen and Wieschaus, 2004; Rauzi et al., 2010). Vinc, Jub, and Cno are also enriched at these high-tension, vertical edges, and at tricellular junctions (TCJs), another contact under high force. Cytoskeletal tension is required for normal Vinc, Jub, and Cno membrane localization, and laser ablation experiments revealed a direct correlation between Vinc enrichment and tension at cell edges (Kale et al., 2018; Razzell et al., 2018; Sawyer et al., 2009, 2011; Yu and Zallen, 2020). The natural variation in tension in the *Drosophila* germband thus provides a model for assessing M region mechanosensing.

Here, we report that the M region is required for cell adhesion during morphogenesis, in particular the M2 domain at contacts that experience higher tension. Our data suggest three distinct tension states read by α-Cat mechanosensing that cause the differential recruitment of Vinc, Jub, and Cno to enhance adhesion. Surprisingly, retention of the M1 domain was more deleterious than removal of the M region entirely. This effect is not due to the recruitment of Vinc, but likely to the M1-dependent regulation of Jub recruitment to AJs. Our findings also support the conclusion that Cno promotes cell adhesion in a parallel pathway to the CCC except at TCJs where M2 and M3 contribute to Cno enrichment. Our work provides evidence of a robust network of cooperative and redundant mechanosensitive interactions at AJs that support tissue morphogenesis.

Results

The M region of α-Cat supports embryonic morphogenesis

We previously analyzed the ability of mutant α-Cat proteins to substitute for endogenous α-Cat in several different *Drosophila* tissues (Sarpal et al., 2012; Desai et al., 2013; Escobar et al., 2015; Ishiyama et al., 2018; Sarpal et al., 2019). Expression of an α-Cat construct that lacks the entire M region (α-Cat-ΔM) could fully support epithelial development of the wing disc epithelium (Sarpal et al., 2019). α-Cat-ΔM also provides strong rescue of *α-Cat* mutant cells of the follicular epithelium (Fig. S1), supports development of the head epidermis and prevents embryonic lethality of most zygotic *α-Cat* null mutant animals (Sarpal et al., 2019). In contrast to the widely considered model that M

region–based mechanosensing enhances adhesion in response to mechanical force (Leckband and De Rooij, 2014; Mège and Ishiyama, 2017; Angulo-Urarte et al., 2020), our in vivo data at this point assigned only a minor or no essential role to the M region in cell adhesion and epithelial development. We therefore wondered whether M region function is most relevant during developmental periods of vigorous morphogenesis when cell contacts experience high levels of force. *Drosophila* gastrulation condenses several large-scale morphogenetic movements into a short ~2-h time window. These movements entail the invagination of the mesoderm and endoderm (Martin, 2020), cell intercalations that drive germband extension (Paré and Zallen, 2020), the ingression of neural stem cells (Simões et al., 2017; An et al., 2017), and three rounds of cell division with a ~40-min cell cycle time (Foe, 1989).

To assess M region function in early embryos, we removed the crucial maternal contribution of *α-Cat* (Sarpal et al., 2012) by RNAi (Fig. S2, A and B) and expressed shRNA-resistant constructs (Sarpal et al., 2019). Our constructs are recruited to AJs (Fig. S2 C) and are expressed at close to normal levels (Desai et al., 2013; Sarpal et al., 2019). Resistant constructs contain a mutated shRNA target site that preserves the amino acid sequence located in the M2 domain (denoted by "R"; e.g., α-CatR, with mutant α-Cat isoforms collectively referred to as α-CatX) or carry a deletion of M2 (Fig. 1 C). Maternally driven *α-Cat-RNAi* caused a dramatic phenotype like that reported for the loss of Arm (Cox et al., 1996) or Ecad (Tepass et al., 1996), leading to a highly fragmented epidermal/cuticle layer (Fig. 1 D). We quantified the cuticle defects, which are indicative of adhesion defects, by counting the number of intact abdominal denticle belts. *α-Cat-RNAi* embryos had 0 intact denticle belts. *α-Cat-RNAi* embryos expressing α-CatR had all eight denticle belts restored in >90% of animals. *α-Cat-RNAi α-Cat-ΔM* animals showed partial restoration of epidermal integrity compared to *α-Cat-RNAi*. Nearly all animals had denticle belt defects, with more than half of embryos producing no denticle belts (Fig. 1, C and D). These results demonstrate a substantive requirement of the M region in maintaining epithelial integrity in the *Drosophila* embryo.

To investigate the function of the M region in early morphogenesis, live embryos were observed during gastrulation with a focus on mesoderm invagination and ectodermal integrity during germband extension. Mesoderm invagination failed in *α-Cat-RNAi* embryos (Fig. 2 A, Fig. S2 A, and Video 1). As previously described (Martin et al., 2010), at the onset of mesoderm invagination actomyosin contraction overpowers residual adhesion in *α-Cat-RNAi* embryos. Cells detached with plasma membrane tethers formed between few remaining AJ puncta (Fig. S2 D). *α-Cat-RNAi α-CatR* embryos showed normal mesoderm invagination. In contrast, *α-Cat-RNAi α-Cat-ΔM* embryos displayed a range of defects. Approximately 40% of embryos showed normal mesoderm invagination where the ventral midline sealed along the entire anterior–posterior axis, whereas the remaining ~60% of embryos showed either a partial closure or a complete failure to close the ventral midline (Fig. 2 A; and Videos 2, 3, and 4).

As the germband starts to extend, ectodermal cells in *α-Cat-RNAi* embryos lose adhesion and large gaps appear between the apical domain of cells (Fig. 2 B). Depletion of the maternal contribution of α-Cat eventually leads to cell dissociation and epithelial collapse (Cavey et al., 2008; Martin et al., 2010; Rauzi et al., 2010; Fernandez-Gonzalez and Zallen, 2011; Wang et al., 2013; Levayer and Lecuit, 2013; Eritano et al., 2020). Similar to the mesoderm, plasma membrane tethers are seen connecting cells across gaps (Fig. S2 E; Fernandez-Gonzalez and Zallen, 2011). *α-Cat-RNAi α-CatR* embryos displayed normal cell contacts, whereas *α-Cat-RNAi α-Cat-ΔM* embryos showed gaps in the epithelium with membrane tethers spanning the gaps (Fig. 2, B and C; and Videos 2, 3, and 4). Apical domains became separated, leading to gaps or tears that extend predominantly along the DV axis (Fig. 2 D). These defects were associated with a marked reduction in germband extension compared to *α-Cat-RNAi α-CatR* controls (Fig. 2 E). Thus, the M region makes an essential contribution to maintaining adhesion during mesoderm invagination and germband extension and its loss compromises these movements.

Retention of M1 is more deleterious to development than removal of the whole M region

We next assessed the performance of α-Cat constructs that lacked individual M region domains (α-CatR-ΔM1, α-Cat-ΔM2, α-CatR-ΔM3) or both M2 and M3 (α-Cat-ΔM23). All constructs analyzed are robustly expressed in embryos, with no defects produced by overexpression in wild-type background (Desai et al., 2013; Sarpal et al., 2019). α-CatR-ΔM1 behaved like full-length α-CatR when we examined the cuticle (Fig. 1 C and Fig. S2 F), mesoderm invagination (stage 6, Fig. 2 A and Video 5), the ectodermal epithelium (Fig. 2, B–D, and Video 5), and germband extension (stages 7 and 8, Fig. 2 E), suggesting that the M1 domain makes no essential contribution to cell adhesion in these tissues. Surprisingly, expression of α-Cat-ΔM23 was much less capable of ameliorating the *α-Cat-RNAi* phenotype than α-Cat-ΔM. *α-Cat-RNAi α-Cat-ΔM23* embryos showed little improvement of the cuticle defects seen with *α-Cat-RNAi* (Fig. 1 C and Fig. S2 F) and failed to rescue mesoderm invagination (Fig. 2 A and Video 6). Most embryos displayed prominent de-adhesion defects in the ectoderm, though these are not as severe as with *α-Cat-RNAi* alone (Fig. 2, B–D, and Video 6), and germband extension was substantially reduced (Fig. 2 E). Rescue by α-Cat-ΔM2 showed minor improvements when compared to α-Cat-ΔM23, whereas expression of α-CatR-ΔM3 showed a much better rescue than α-Cat-ΔM2 (Fig 1 C, Fig. 2, Fig. S2 F, and Videos 6, 7, and 8). This suggests that M2 is the most important domain within the M region for supporting cell adhesion, with M3 making a minor contribution. Notably, the poor rescue activity seen with α-Cat-ΔM23 compared to α-Cat-ΔM suggests that the M1 domain, which is predicted to remain unfurled in α-Cat-ΔM23, negatively regulates cell adhesion.

The M region contributes to cell adhesion at medium- and high-tension cell contact sites

The ectoderm during germband extension displays an asymmetric distribution of non-muscle myosin II, which is enriched at vertical cell edges (oriented along the DV axis) and at TCJs. Laser ablation of junctions produces higher retraction velocities

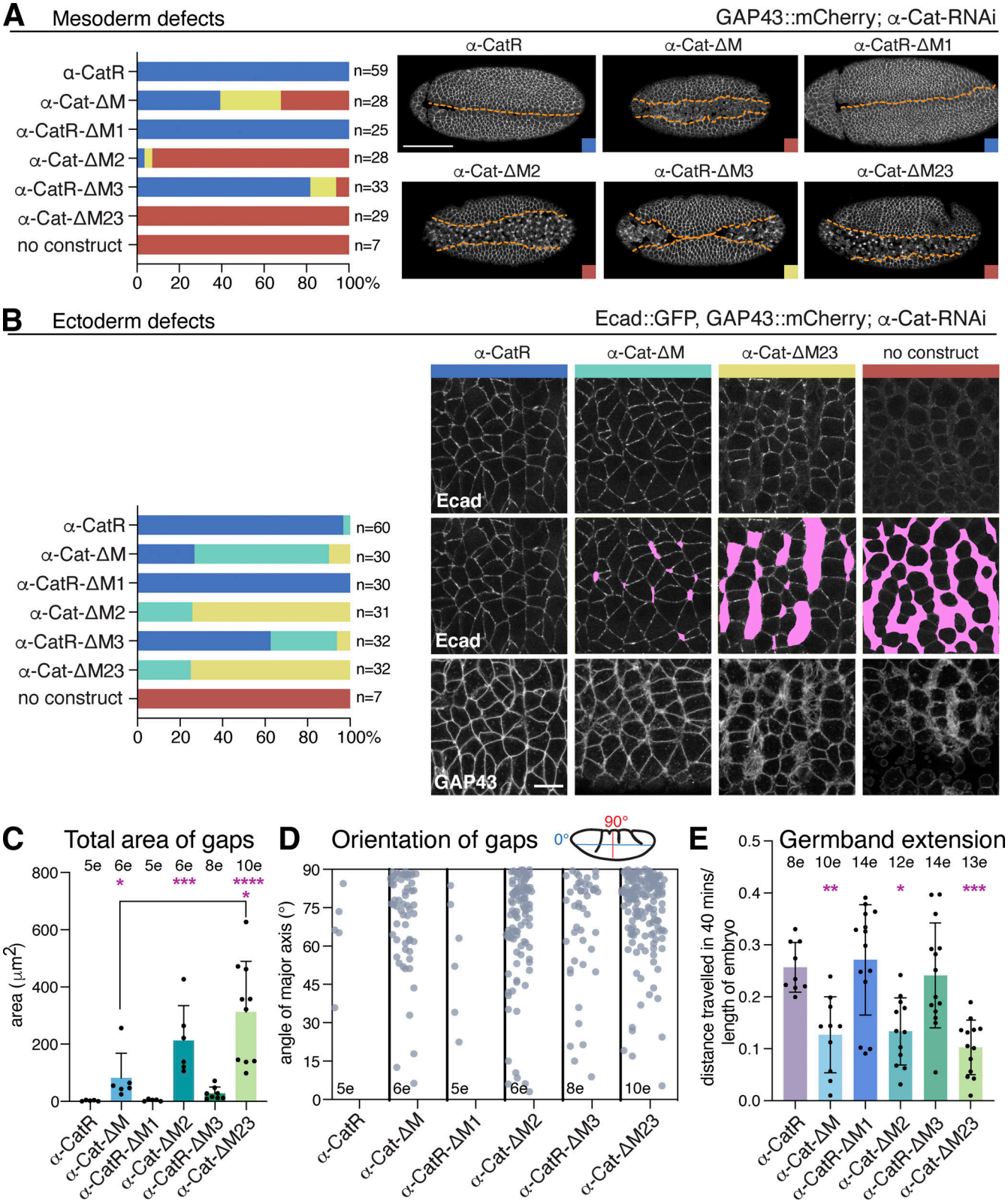

Figure 2. **The α-Cat M region is essential for adhesion during mesoderm invagination and germband extension. (A)** Quantification of mesoderm invagination defects in embryos of indicated genotype. Color-coded example images are given at right. Orange lines indicate edges of mesoderm. Red, open ventral furrow; yellow, partially fused ventral furrow; indigo, >90% midline fusion. Scale bar; 100 µm. **(B)** Quantification of defects in the lateral ectoderm during germband extension in embryos of indicated genotype. Classification used: indigo, wild type, very few gaps seen; cyan, small gaps; yellow, large gaps or tears; red, few if any identifiable AJs. Pink areas represent regions of gaps where apical junctions have lost contact, plotted in C. Scale bar, 10 µm. **(C)** Area of gaps in *α-Cat-RNAi α-CatX* embryos. *n* is the sum of all gap areas within a field of view per embryo (e). **(D)** Plot showing the angle of the major axis of ellipses

fitted to each gap in *α-Cat-RNAi α-CatX* embryos. *N* = number of embryos (e), 90° = DV axis. **(E)** Extension of the germband observed over 40 min in *α-Cat-RNAi α-CatX* embryos. Change in length from proctodeal invagination to posterior is normalized to total embryo length; *n* = number of embryos analyzed (e). For C and E, height of bars represent mean, error bars represent SD. Significance determined by Kruskal–Wallis test with Dunn's multiple comparisons test (C), and ordinary one-way ANOVA with Tukey's multiple comparisons test (E; **** = P < 0.0001, *** = P < 0.001, ** = P < 0.01, * = P < 0.05).

in myosin-rich vertical edges versus horizontal edges, and modeling predicts that TCJs show the highest tension (Bertet et al., 2004; Zallen and Wieschaus, 2004; Fernandez-Gonzalez et al., 2009; Tetley et al., 2016; Vanderleest et al., 2018; Higashi and Miller 2017; Trichas et al., 2012). For the purpose of our discussion and reflecting the distribution of myosin, we distinguish between low-tension horizontal bicellular junctions (BCJs), medium-tension vertical BCJs, and high-tension TCJs (vertices). Contraction of myosin at vertical edges either in multicellular rosettes or at bicellular contacts are important drivers of cell intercalation required for germband extension (Zallen and Wieschaus, 2004; Blankenship et al., 2006; Zallen and Blankenship, 2008; Fernandez-Gonzalez et al., 2009; Tetley et al., 2016; Vanderleest et al., 2018) and neuroblast ingression (Simões et al., 2017). We noticed that gaps or tears in the epithelium of embryos expressing M region deletions were commonly found at the centers of rosettes or at vertices, and were elongated along the DV axis (Fig. 2, B and D). These findings further suggest that the M region and its individual domains, except for M1, strengthen adhesion and that medium and high-tension cell contacts are more susceptible to loss of adhesion than other cell contacts.

To further characterize these adhesion defects, we analyzed the actomyosin cytoskeleton using the endogenously YFP-tagged myosin heavy chain. The expression of any M region deletion in an *α-Cat-RNAi* background led to increased total myosin signal (Fig. 3, A and E), while the enrichment of myosin to vertical edges was consistently observed (Fig. 3 A). As myosin is recruited by tension (Fernandez-Gonzalez et al., 2009) this suggests that the asymmetric distribution of tension in the ectoderm is not strongly affected in embryos expressing M region deletions. Although membrane association of myosin was preserved even with a poor rescue of adhesion as in *α-Cat-RNAi α-Cat-ΔM23* embryos, separation of apical domains along the DV axis led to the apparent splitting of supracellular myosin cables (Fig. 3 B). In embryos with stronger defects, myosin accumulates in large puncta at the free apical cell edges of gaps after they had formed (Fig. 3 B).

Gaps in the ectoderm of *α-Cat-RNAi α-CatX* embryos could also be visualized by an enhanced signal of the active Rho1 probe Ani-RBD. Activation of Rho1 causes the phosphorylation of myosin regulatory light chain by Rho kinase, and hence myosin contraction, with enrichment of active Rho1 seen at sites of high actomyosin contractility in the germband (Munjal et al., 2015; Martino et al., 2018). Loss of apical cell contact was followed by the formation of large puncta of Ani-RBD (Fig. 3, C and D), which is enriched along the perimeter of epithelial gaps (Fig. 3 F). These observations are reminiscent of the accumulation of active Rho1 and myosin at wound margins (Abreu-Blanco et al., 2014; Rothenberg and Fernandez-Gonzalez, 2019), and Rho flares, which repair breaches in the epithelial barrier during *Xenopus* development (Stephenson et al., 2019). The appearance of membrane tethers (Fig. 2 B) and the accumulation of active Rho1 and myosin (Fig. 3) confirmed the loss of cell–cell contacts within the germband, particularly at medium- and high-tension cell edges or vertices, for embryos expressing deletions that remove the M2 domain (Fig. 2, B and C; and Fig. 3 C). Moreover, α-CatR-ΔM3 and α-Cat-ΔM23 expressing embryos showed comparatively lower levels than α-CatR in both cortical Ani-RBD signal and the proportion of junctional myosin (Fig. 3, E and F). In contrast, a higher fraction of junctional myosin was seen when M1 was deleted (Fig. 3 E). Together, these findings suggest that the M region contributes to the regulation of junctional actomyosin.

M2/3 and M1 play opposing roles in regulating AJs

To further characterize the impact of the M region on cell adhesion, we examined the junctional distributions of Ecad, Vinc, and Jub using fluorescently tagged proteins under the control of their endogenous promoters (Huang et al., 2009; Sabino et al., 2011; Kale et al., 2018). In *α-Cat-RNAi α-CatX* embryos, the levels of Ecad correlated with the strength of adhesion defects observed (Fig. 4, A and C; for a summary of results, see Fig. 4 D), with lower levels of Ecad associated with more severe defects, as expected. Removal of M2 or M3 caused a significant reduction of cortical Ecad, suggesting that these domains predominantly contribute to the stability of the CCC at the junction (Fig. 4, A, C, and D). This concurs with a reduction of junctional Arm in wing disc cells lacking M2 or M3 (Sarpal et al., 2019). In contrast, the M1 domain has an inhibitory effect on Ecad. *α-Cat-RNAi α-CatR-ΔM1* embryos showed elevated cortical enrichment of Ecad (Fig. 4, A, C, and D), consistent with an increase in junctional Arm in α-CatR-ΔM1 expressing wing disc epithelium (Sarpal et al., 2019; Alégot et al., 2019). An increase in Ecad levels as a result of the absence of M1 was also seen when comparing α-Cat-ΔM23 and α-Cat-ΔM embryos, and α-Cat-ΔM appears to be better maintained at the membrane and is less punctate than α-Cat-ΔM23 (Fig. 4 and Fig. S2 A). We conclude that the M region regulates junctional stability with M1 and M2/3 having opposing effects. Whereas M2/3 stabilizes the junction, M1 limits junctional Ecad.

M2 and M3 negatively regulate M1 function

Although direct binding between Vinc and *Drosophila* α-Cat is yet to be assessed in vitro, we found that M1 is required for all detectable junctional Vinc signal in gastrulating embryos (Fig. 4, A, C, and D). As removal of M2 and M3 also reduces Ecad, which is expected to reduce recruitment of AJ proteins, we wanted to know whether the reduction in Vinc in these conditions is explained by a reduction of the CCC. We therefore calculated the ratio of cortical Vinc to Ecad per cell (expressed within the same embryo). We found that the M2 and M3 domains contribute to

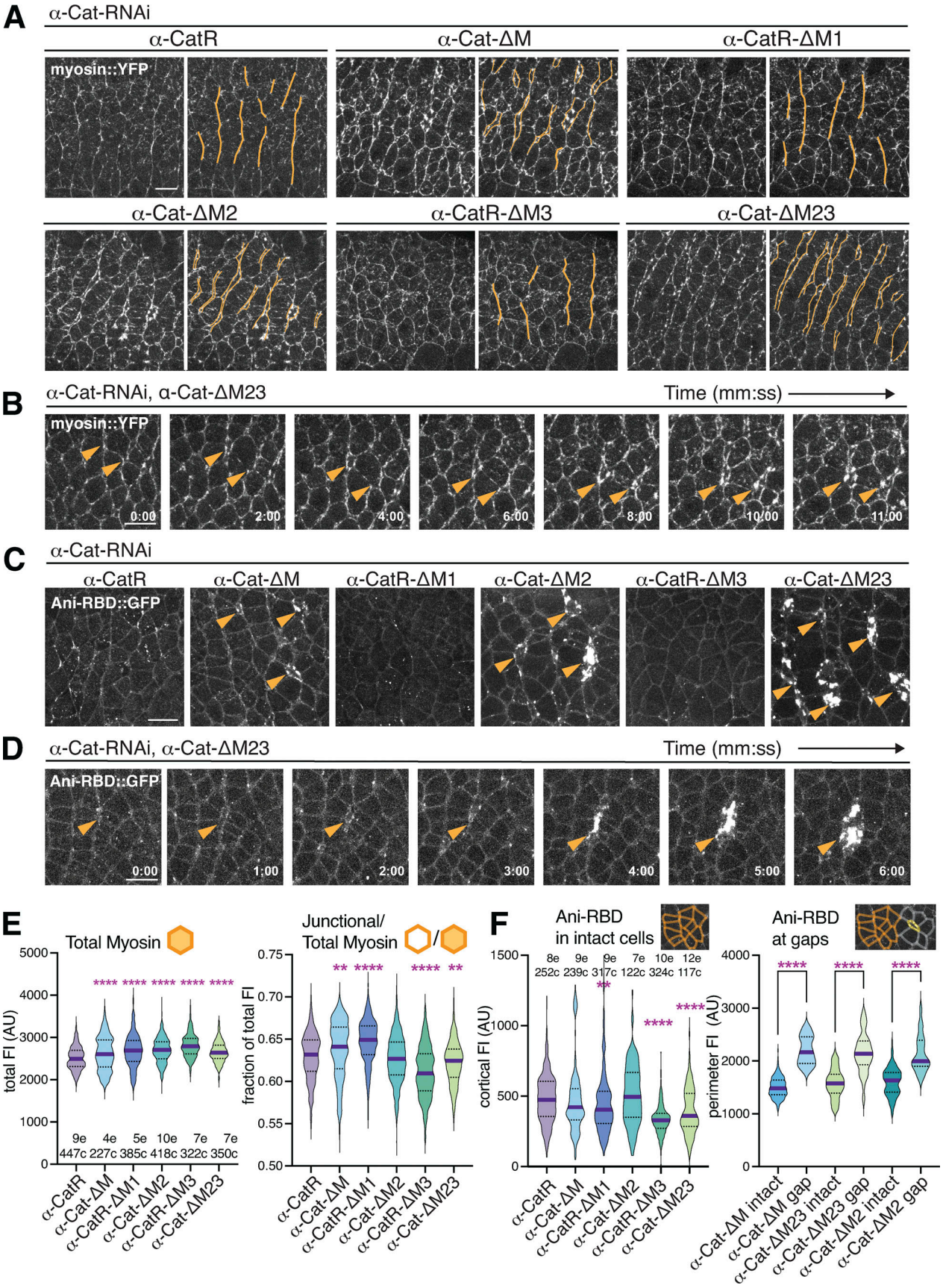

Figure 3. **Myosin distribution and Rho1 activity in embryos expressing α-Cat M region deletions. (A)** Representative images of ectoderm during germband extension of *α-Cat-RNAi α-CatX* embryos. Myosin cables are highlighted with orange lines in the right duplicate images. **(B)** Series of stills from a live

α-Cat-RNAi α-Cat-ΔM23 embryo showing gaps forming at vertical edges (arrowheads) with accumulations of myosin at gap perimeters. **(C)** Stills from live *α-Cat-RNAi α-CatX* embryos expressing the Rho1 activity probe, Ani-RBD::GFP. Note accumulation of Ani-RBD::GFP in gap areas (arrowheads). **(D)** Series of stills from a live *α-Cat-RNAi α-Cat-ΔM23* embryo showing enrichment of Ani-RBD::GFP at a gap between cells (arrowheads). Cell contacts first split and subsequently Ani-RBD signal increases. **(E)** Quantification of total myosin (cytoplasmic and junctional) and junctional myosin as a fraction of total myosin in *α-Cat-RNAi α-CatX* embryos. **(F)** Quantification of Ani-RBD::GFP signal at cortices of cells which are not in contact with a gap (intact). At right, mean FI of Ani-RBD::GFP signal at the perimeter (with no subtraction of cytoplasmic FI) of cells with intact junctions is compared to the perimeter of gaps (for Ani-RBD at gaps, significance determined by Mann-Whitney two-tailed test). For E and F, significance is determined by Kruskal–Wallis test with Dunn's multiple comparisons test (**** = P < 0.0001, ** = P < 0.01). *n* = pooled number of cells (c) from number of embryos (e). Bold line, median; dotted lines, interquartile ranges. Scale bar in A–D, 10 µm. Schematics above plots describe measurement used in this and following figures (see Fig. S5 for legend).

Vinc junctional levels even when normalized to the amount of remaining Ecad (Fig. 4, A, C, and D). Removal of both M2 and M3 together significantly increases the Vinc/Ecad ratio compared to α-CatR control (Fig. 4, A, C, and D). Together, this suggests that both M2 and M3 individually inhibit M1, but also each other, such that removing M2 and M3 together relieves all inhibition of Vinc junctional recruitment (Fig. 4 E). Removing M2 alone leaves M3 free to inhibit the M1–Vinc interaction and vice versa. This agrees with work using cells in culture identifying a masking effect between domains (Yonemura et al., 2010; Matsuzawa et al., 2018; Sakakibara et al., 2020), and provides evidence within an animal model to support the existence of autoinhibition among M region domains.

M1 inhibits the α-Cat–Jub interaction during germband extension

Embryos where M1 is removed showed a dramatic increase in Jub at the junctions (Fig. 4, B–D). In contrast, Jub levels are reduced in *α-Cat-RNAi* embryos expressing α-Cat-ΔM2, α-CatR-ΔM3, or α-Cat-ΔM23, suggesting that the M2 and M3 domains support junctional Jub. Despite lacking M2 and M3, embryos expressing α-Cat-ΔM experience an enrichment of Jub (Fig. 4, B–D). Thus, as shown for the wing disc epithelium (Sarpal et al., 2019; Alégot et al., 2019), M1 also acts as an inhibitor of junctional Jub recruitment in the embryonic ectoderm. Retention of the M1 domain in *α-Cat-RNAi α-Cat-ΔM23* embryos produces the largest reduction in Ecad, Jub (Fig. 4), and the strongest adhesion defects (Fig. 1 C, Fig. 2, and Fig. S2 F). As junctional Jub has a positive role in cell adhesion in the ectoderm (Razzell et al., 2018), we conclude that M1 is a negative regulator of cell adhesion, a role normally limited by the functions of M2 and M3, an inhibition resolved by the force-dependent unfurling of the M region.

The M2 domain is required for the mechanosensitive enrichment of Jub at high-tension edges

We also found that manipulation of the M region significantly affected the mechanosensitive recruitment of Jub. Jub is recruited to the membrane in response to cytoskeletal tension (Rauskolb et al., 2019; Razzell et al., 2018; Alégot et al., 2019). In wing disc epithelium, removal of the M1 domain causes Jub to become hyper-recruited to junctions without an increase in tissue tension (Sarpal et al., 2019; Alégot et al., 2019). How this occurs is unclear as the Jub-binding site is not within the M region, but in the N2 domain (Marie et al., 2003; Alégot et al., 2019; Sarpal et al., 2019). A requirement for the α-Cat N-terminal domain for the junctional recruitment of Jub was confirmed in the embryo, as rescue with a construct that lacks this domain (DEcadΔβ::α-Cat-ABD) depleted Jub levels to the same degree as α-Cat knockdown (Fig. 5, A–C).

During germband extension, vertical edges are under higher tension than horizontal contacts (Fernandez-Gonzalez and Zallen, 2011). As Jub signal increases with increasing tension, this leads to the planar polarized enrichment of Jub at vertical edges (Razzell et al., 2018). Similarly, Vinc and Cno localization depend on cytoskeletal tension and are also planar polarized (Hara et al., 2016; Kale et al., 2018; Sawyer et al., 2011; Yu and Zallen, 2020). The mean fluorescent intensity (FI) of Vinc, Jub, and Cno increases in accordance with expected relative tension in the embryo, lowest at horizontal BCJs, higher at vertical BCJs and highest at TCJs (Fig. 5 D). This provided us with a system in which we could test Jub response to tension. We determined the planar polarity of Jub in *α-Cat-RNAi α-CatX* embryos by measuring the average FI of Jub along vertical edges (Fig. 5 C), divided by that of horizontal edges (Fig. 5 B) within the same embryo (Fig. 5 E). This analysis revealed that the M2 domain is in fact required for the specific enrichment of Jub to vertical cell contacts. Expression of α-Cat-ΔM, α-Cat-ΔM23, and α-Cat-ΔM2 failed to rescue the enrichment of Jub to edges approaching 90° (where the anterior–posterior axis = 0°), and in some instances a reversal of Jub planar polarity was seen with higher Jub levels at horizontal versus vertical edges (Fig. 5 E and Fig. S3 A). Furthermore, in all experimental conditions, Jub levels at TCJs versus BCJs were reduced as compared to control (Fig. 5 F). The M region is thus required for the tension-dependent distribution of Jub.

In *α-Cat-RNAi α-Cat-ΔM1* embryos, Jub planar polarity and enrichment at TCJs is significantly reduced, but in this case is due to a constitutive enrichment of Jub to all cell contacts, regardless of the state of tension (Fig. 5, A–C and E; and Fig. S3 A). Similarly, in wing disc epithelium, loss of M1 desensitizes junctional Jub recruitment to a reduction of myosin activity (Alégot et al., 2019). The planar polarity of Jub thus requires M2 for the mechanosensitive recruitment to higher-tension edges, while M1 limits Jub at lower-tension edges. Only at the highest tension sites, at TCJs, was a role for M3 alone seen in supporting Jub enrichment (Fig. 5 F). Although Jub is required for normal germband extension, its planar polarity is not essential for adhesion or germband extension (Razzell et al., 2018). M2 and M3 may therefore function by supporting the necessary amount of Jub at higher-tension edges, and hence support Ecad membrane stability against enhanced actomyosin contractility. As junctional Jub is more enriched in α-Cat-ΔM than α-Cat-ΔM23 embryos, we wondered whether the lack of M1-mediated inhibition

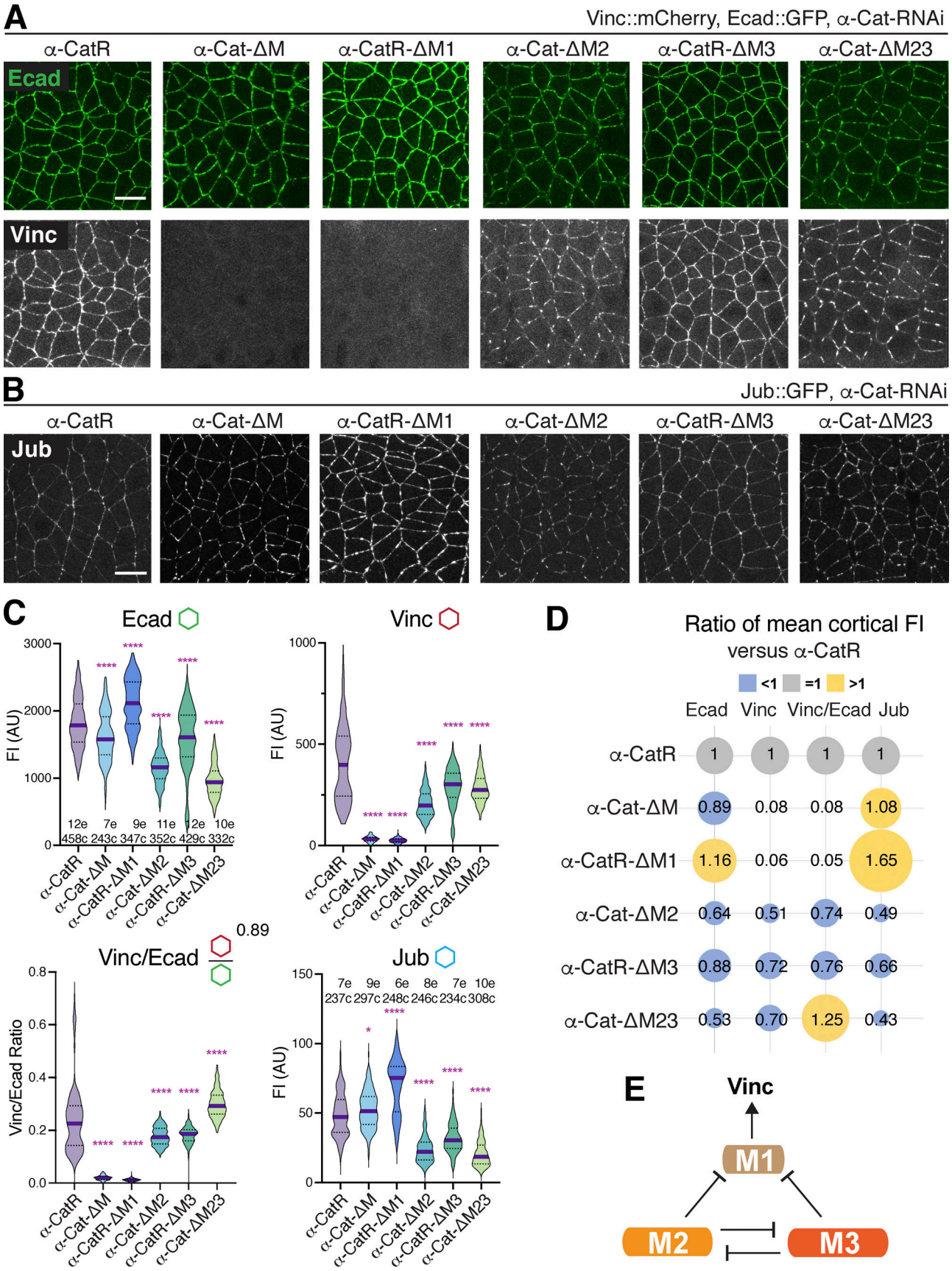

Figure 4. **The M region regulates the levels of AJ components. (A)** Stills of live *α-Cat-RNAi α-CatX* embryos at stage 8 (rapid phase of germband extension, 3:10–3:40 h after egg laying) expressing Ecad::GFP and Vinc::mCherry. **(B)** Stills of live *α-Cat-RNAi α-CatX* embryos at stage 8 expressing Jub::GFP. Scale bar for

A and B, 10 µm. **(C)** FIs of junctional signal of Vinc::mCherry, Ecad::GFP, and Jub::GFP in *α-Cat-RNAi α-CatX* embryos at stage 8. The ratio of cortical Vinc to Ecad per cell is given as Vinc/Ecad. *n* = a pooled number of cells (c) from a number of embryos (e); Ecad, Vinc, and Vinc/Ecad are measured from the same cells. Bold line, median; dotted lines, interquartile ranges. Significance calculated by Kruskal–Wallis test with Dunn's multiple comparison test for Ecad, Vinc, and Vinc/Ecad and ordinary one-way ANOVA with Tukey's multiple comparison test for Jub (**** = P < 0.0001, * = P < 0.05). **(D)** Balloon plot summarizing changes in mean junctional fluorescent signals. **(E)** Schematic illustration of the functional relationship between M1, M2, and M3 in respect to the recruitment of Vinc to the AJ.

of Jub helps to explain the difference in rescue of cell adhesion by these two constructs. Indeed, depletion of Jub by RNAi worsened epithelial integrity of *α-Cat-RNAi α-Cat-ΔM* embryos (Fig. 5 H). These results suggest that Jub and the M2/3 domain cooperate with each other to support AJs under morphogenetic stress and underline a requirement for M2/3 in the mechanosensitive recruitment of Jub to junctions under higher tension (Fig. 5 I).

The M region reinforces Ecad against enhanced actomyosin contraction

In contrast to the enrichment of the α-Cat interaction partners Jub, Vinc, and Cno at vertical, high-tension edges during germband extension (Blankenship et al., 2006; Sawyer et al., 2011; Kale et al., 2018; Razzell et al., 2018), AJ components such as Baz, Arm, α-Cat, and Ecad become planar polarized and enriched at horizontal edges (Paré and Zallen, 2020). Within an Ecad::GFP, GAP43::mCherry background, embryos expressing *α-Cat-RNAi α-Cat-ΔM* and *α-Cat-RNAi α-Cat-ΔM23* showed significantly enhanced planar polarized localization of Ecad. Ecad was reduced specifically from the actomyosin-enriched vertical edges compared to α-CatR controls (Fig. 6 A), suggesting that the M2 and M3 domains support Ecad at high-tension edges. Interestingly, within an Ecad::GFP, Vinc::mCherry background, a reversal of Ecad planar polarity was seen in *α-Cat-RNAi α-Cat-ΔM23* embryos (in which Vinc is ectopically enriched per CCC), while there was no change to Ecad planar polarity in embryos rescued by α-Cat-ΔM or α-CatR-ΔM1 (which Vinc is not predicted to bind; Fig. 6 A). Expression of Vinc::mCherry to assess Vinc distribution provided an additional genomic copy of Vinc, representing an over-expression condition. This additional copy of Vinc also improves adhesion in the ectoderm of *α-Cat-RNAi α-Cat-ΔM23* embryos compared to controls without Vinc::mCherry (Fig. 6 B). Total gap areas in *α-Cat-RNAi α-Cat-ΔM* embryos are not significantly changed by additional Vinc (Fig. 6 B), suggesting this role for Vinc is mediated through its interaction with the CCC. As another method to enhance Vinc activity, we expressed an active, constitutively open form of Vinc (Vinc-CO; Maartens et al., 2016). This caused a strong enrichment of Ecad (Fig. 6 C), and a reversal of Ecad planar polarity such that Ecad is enriched at vertical edges (Fig. 6 D). These results suggest that the M1–Vinc interaction can reinforce Ecad recruitment or stability in response to actomyosin contraction and, consequently, cell adhesion during *Drosophila* gastrulation (Fig. 6 I). However, as the M1 domain is dispensable for adhesion and embryonic development, it is unlikely that the recruitment of Vinc is the primary mode of junctional reinforcement through the M region in wild type. Instead, our data suggests that M1 functions as an inhibitor of AJs.

The M1 domain is required for the normal distribution of Ecad through recruitment of Vinc

Since M1 has an inhibitory effect on Ecad and Jub, and retention of M1 both enriches Vinc and causes more severe defects than removal of the whole M region, we wondered whether Vinc has an inhibitory effect on Ecad or Jub, and thus adhesion. A *Vinc* null mutant allele was incorporated into the rescue set-up to see if this would ameliorate epithelial integrity defects in *α-Cat-RNAi α-Cat-ΔM23* embryos. However, removal of Vinc in fact worsened the defects in α-Cat-ΔM23 embryos, suggesting that Vinc cooperates with the M2 and M3 domains to support adhesion (Fig. 6 E). Furthermore, we confirmed that *Vinc* null mutants have no discernable epithelial defects during gastrulation, as previously reported (Alatortsev et al., 1997; Maartens et al., 2016), but found subtly yet significantly reduced α-Cat and Jub levels (Fig. 6, F and H). Although M1 is similarly dispensable for embryonic development, abnormally large clusters of Ecad, Jub, and α-Cat-ΔM1 were seen in *α-Cat-RNAi α-Cat-ΔM1* embryos along AJs compared to α-CatR expressing controls (Fig. 5 A, Fig. 6 G, and Fig. S4 A). We used the normalized SD of Ecad to estimate the fragmentation of junctional signal, and this was significantly increased in the absence of M1 (Fig. 6 G). Likewise, junctional α-Cat signal is more fragmented in *Vinc* embryos (Fig. 6 H). M1 recruitment of Vinc therefore does support a more uniform distribution of the CCC at AJs, but the impact of its loss has no apparent phenotypic consequences. Overall, our observations suggest that the inhibitory effect the M1 domain has on adhesion is not due to Vinc recruitment, and that the M1 domain plays a dual inhibitory and supportive role at AJs.

Cno requires M2/3 for its enrichment at TCJs, but is cortically recruited independently of the α-Cat M region

Loss of either Vinc or Jub alone did not produce significant adhesion defects in *Drosophila* embryos (Maartens et al., 2016; Razzell et al., 2018), and Jub knockdown in a *Vinc* mutant background did not enhance embryonic lethality. However, loss of Vinc or Jub enhanced epithelial defects in M region deletion construct expressing embryos (Fig. 5 E and Fig. 6 E), raising the possibility that they work in parallel with an additional interaction partner of the M region, contributing to its mechanosensory output. As Afadin binds the mammalian α-catenin M2/3 domains (Pokutta et al., 2002; Sakakibara et al., 2020), we were wondering whether force-dependent junctional localization of Cno could help explain M region function in cell adhesion.

A direct M3–Afadin interaction was reported in MDCK cells, which is inhibited by M1 (Sakakibara et al., 2020). Although direct interactions between *Drosophila* Cno and α-Cat have not been reported to date, we found that removal of either M3 or M1 led to an increase in cortical Cno (Fig. 7, A and B). In fact, cortical Cno, representing largely the bicellular Cno pool, increased

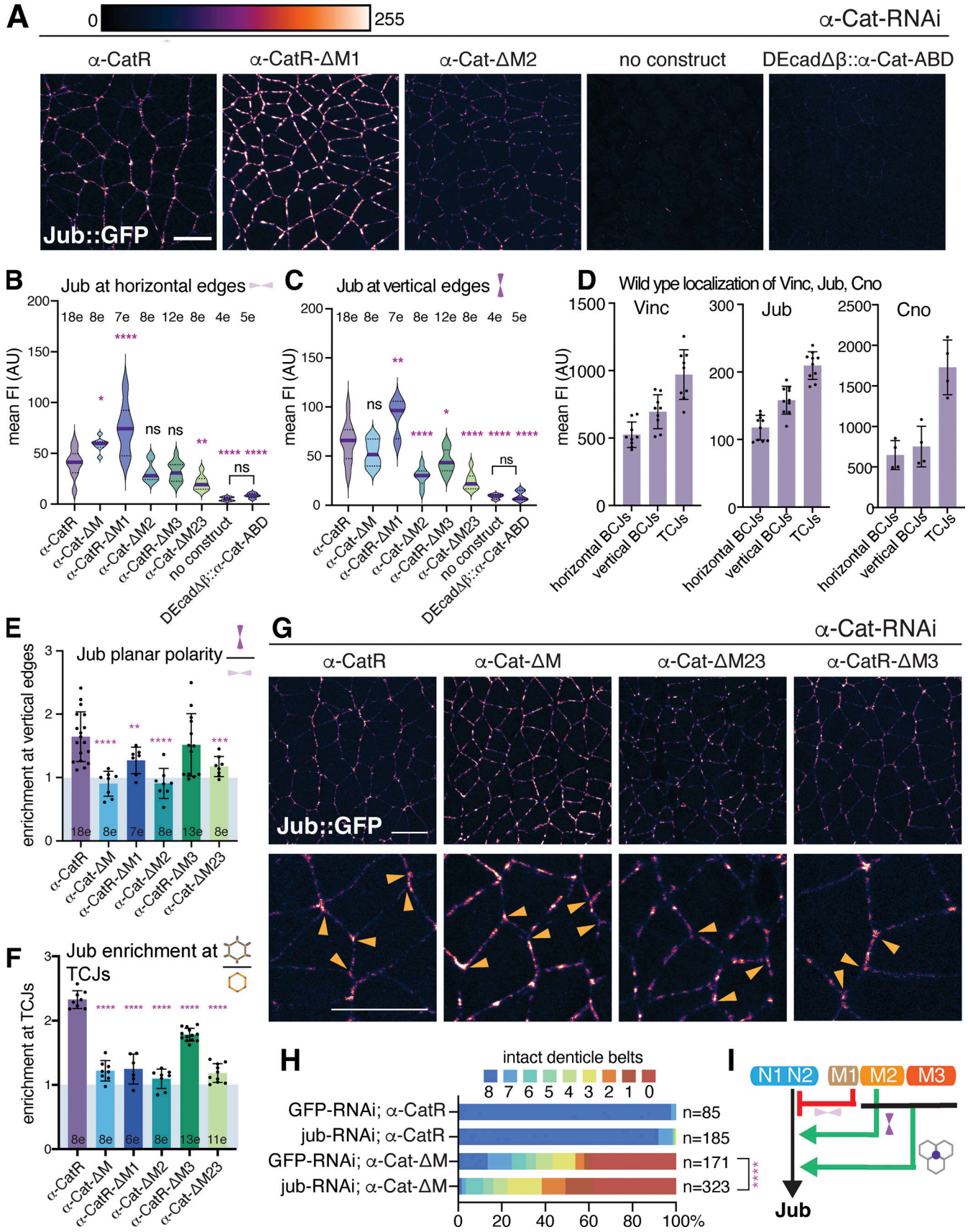

Figure 5. **M region supports mechanosensitive recruitment of Jub to AJs. (A)** Stills from live *α-Cat-RNAi α-CatX* embryos expressing Jub::GFP. FI is displayed as shown in color map at top. Maximum FI (255), white. Scale bar, 10 µm. **(B and C)** The mean FI of Jub (with background cytoplasmic signal subtracted)

for *α-Cat-RNAi α-CatX* embryos at stage 8 is plotted for (B) horizontal edges (0–15°) and (C) vertical edges (75–90°; 90° = DV axis). *n* = number of embryos (e); bold line, median; dotted lines, interquartile ranges. Significance determined by ordinary one-way ANOVA with Tukey's multiple comparisons test. **(D)** Mean FI of Vinc, Jub, Cno at horizontal BCJs, vertical BCJs, and TCJs in stage 8 embryos. Points represent mean FI of regions of interest per embryo (for Vinc, *n* = 9; Jub, *n* = 9; Cno *n* = 4). **(E)** Quantification of planar polarity of Jub is plotted per embryo as mean FI of vertical edges divided by that of horizontal edges, derived from data in B and C. Significance determined by ordinary two-way ANOVA with uncorrected Fisher's LSD for all bins. See Fig. S3 for more detailed breakdown of enrichment of FI by angles of edges. **(F)** Quantification of enrichment of Jub signal at TCJs vs. BCJs within the same embryo. Significance determined by ordinary one-way ANOVA with Tukey's multiple comparison test. For D, E, and F, height of bars represents mean, and error bars represent SD. **(G)** Live-imaged stills of *α-Cat-RNAi α-CatX* embryos expressing Jub::GFP, with close-ups highlighting TCJs (orange arrowheads). Scale bar, 10 µm; color map same as in A. **(H)** Analysis of cuticle defects of *α-Cat-RNAi α-CatX* embryos and either *GFP-RNAi* as a control or *Jub-RNAi*. Number of embryos analyzed = *n*. Significance determined by Chi-square test. For B, C, E, F, and H, **** = P < 0.0001, *** = P < 0.001, ** = P < 0.01, * = P < 0.05. **(I)** Schematic summary: Junctional recruitment of Jub depends on the interaction between Jub and the N2 domain. This interaction is inhibited at horizontal edges by M1 and is supported at higher tension vertical edges by M2, and at TCJs by M2 and M3.

modestly with the expression of all M region deletions except for α-Cat-ΔM23, which showed a reduction but not a loss of Cno at AJs (Fig. 7, A and B). At gastrulation, Cno is significantly reduced by the knockdown of α-Cat (Fig. 7, A and B), when few cell junctions remain. Since Cno levels are increased in α-Cat-ΔM expressing embryos, the reduction of Cno in *α-Cat-RNAi α-Cat-ΔM23* embryos may be a consequence of the strong adhesion defects in this condition. These observations suggest that Cno has alternate means of junctional recruitment, in particular at BCJs, apart from M region interactions. Deletion of M1 is predicted to unmask M2 and M3, but bicellular α-Cat-ΔM1 signal does not colocalize better with Cno than α-CatR control when expressed in *α-Cat-RNAi* embryos (Fig. S4, A and B), further supporting the conclusion that Cno can localize to BCJs independently of the M region. Echinoid (Ed) is thought to cooperate with Ecad to support Cno recruitment in the wing disc (Wei et al., 2005; Sawyer et al., 2009). However, even in a tissue that does not express Ed, the amnioserosa (Lin et al., 2017), junctional recruitment of Cno was not depleted in *α-Cat-RNAi α-CatR-ΔM3* or *α-Cat-RNAi α-Cat-ΔM* embryos (Fig. S4 C). Knockdown of Ed in *α-Cat-RNAi α-Cat-ΔM* embryos also did not produce noticeable changes in phenotype (Fig. S4 D). Furthermore, α-Cat constructs were consistently located more basally than Cno in germband BCJs (Fig. S4 E). We also found that Cno enrichment at medium-tension vertical BCJs was not reduced in *α-Cat-RNAi α-Cat-ΔM* and *α-Cat-RNAi α-Cat-ΔM23* embryos (Fig. 7 E and Fig. S3 A). Together, these findings suggest that pathways independent of Ed and α-Cat regulate the association of Cno with BCJs in the embryonic ectoderm.

Cno is normally elevated both at vertical BCJs during gastrulation and at TCJs (=vertices; Sawyer et al., 2009; Sawyer et al., 2011; Fig. 5 D). Interestingly, enrichment of Cno at TCJs, but not BCJs, is responsive to cytoskeletal tension (Yu and Zallen, 2020). We assessed Cno levels at vertices as a TCJ/BCJ ratio within the same embryo. Although the minimal Afadin binding site of αE-catenin is located within M3 (Pokutta et al., 2002; Sakakibara et al., 2020), removing M3 alone had no effect on the TCJ enrichment of Cno (Fig. 7, A and D). The enrichment of Cno at vertices was significantly reduced in embryos lacking M2, and this is worsened when M3 is also removed (Fig. 7, A, D, and E). However, some enrichment under M2/3 deletion is not abolished (Fig. 7, C and D) suggesting that M2/3 is not solely responsible for Cno recruitment to TCJs. Our results suggest that M3 along with M2 support normal levels of Cno recruitment to TCJ but that the M region is not involved in the localization of Cno to BCJ (Fig. 7 I).

Vertices maximize α-Cat mechanosensing

Some vertices experience actomyosin forces from more than three junctions during the cell intercalations associated with germband extension. Each junction shows actomyosin generated tension (Fernandez-Gonzalez et al., 2009), predicting that connecting additional junctions increases the force at the vertex. We took advantage of this and compared vertices with three junctions to vertices with four or five junctions that are frequently observed in rosettes (Blankenship et al., 2006). In control *α-Cat-RNAi α-CatR* embryos, we found that Ecad is reduced as the number of junctions connected to a vertex increases (Fig. 7 H), suggesting that an increased number of edges linked to a vertex increasingly challenges the AJ. Interestingly, Jub enrichment increased only slightly with the number of junctions connected to a vertex (Fig. 7 G), whereas Cno remained unchanged when three, four, and five junction vertices were compared in *α-Cat-RNAi α-CatR* embryos (Fig. 7 F). In contrast, vertex enrichment of Cno and Jub dropped significantly in embryos expressing α-Cat-ΔM or α-Cat-ΔM23 (Fig. 7, F and G). Embryos lacking M2 and M3 showed a reduction in Cno, Jub, Vinc, and Ecad enrichment at all vertices, with a loss of Jub, Vinc, and Ecad enrichment at vertices joining four and five junctions (Fig. 7, F–H and Fig. S3 C). Vertices joining five edges showed Cno levels lower than BCJs in *α-Cat-RNAi α-Cat-ΔM23* embryos (Fig. 7 F). Taken together, these findings suggest that although Cno membrane recruitment occurs independently of the α-Cat M region, the enrichment of Cno at vertices requires an interaction with the α-Cat M2 and M3 domains, and these domains support AJ stability at vertices to resist the increasing forces vertices experience during cell intercalation (Fig. 7 I). Moreover, the lack of progressive enrichment of Jub and Cno when three, four, and five junction vertices are compared would be consistent with a model posing that virtually all α-Cat molecules at a three-junction vertex are in an open conformation, maximizing the mechanosensitive recruitment at these sites that cannot further be enhanced by increasing force.

Cytoskeletal tension elicits the M region–dependent junctional recruitment of Jub and Cno

To further test the hypothesis that the M region supports the mechanosensitive recruitment of Jub and Cno, we manipulated

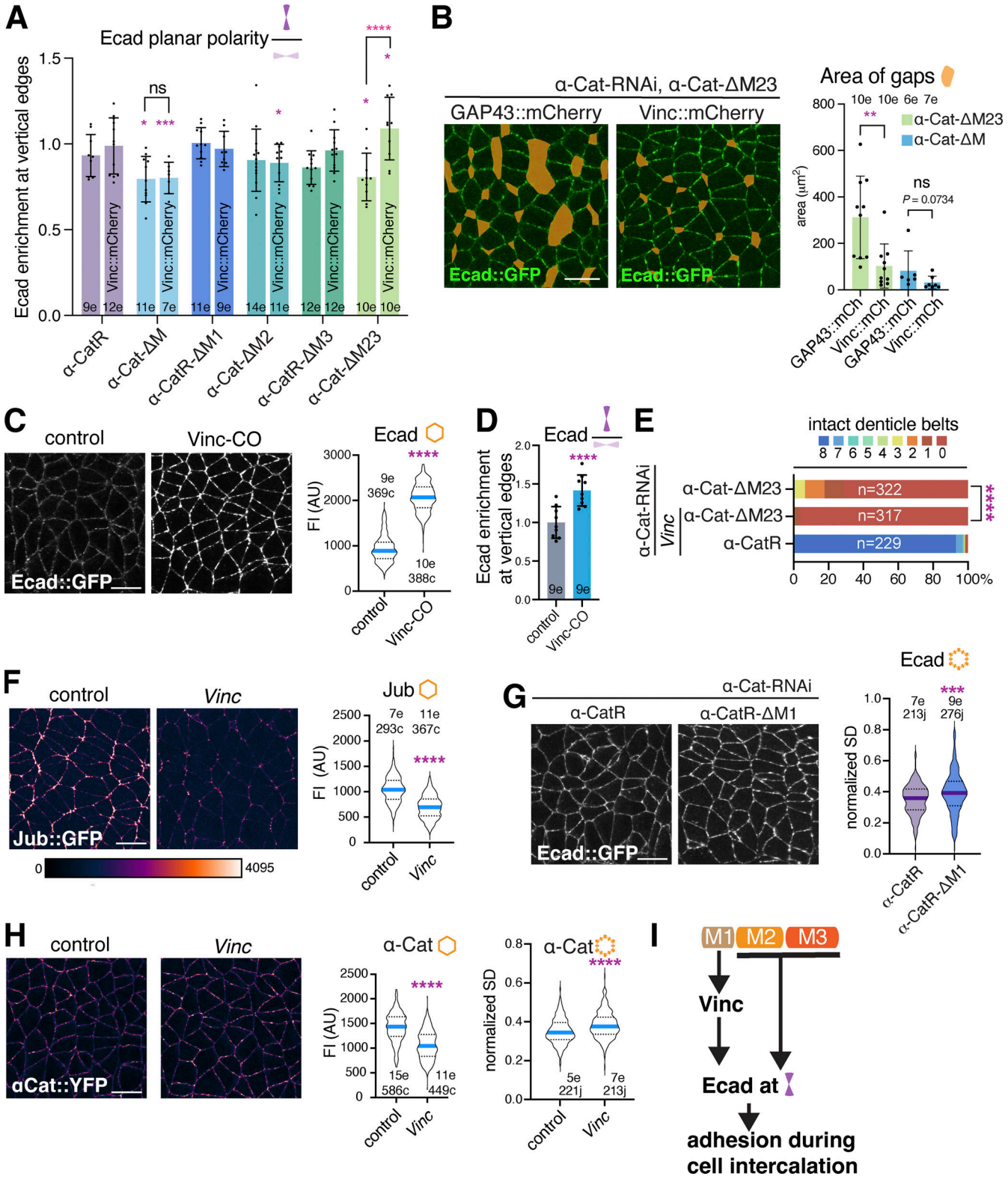

Figure 6. **The M1–Vinc interaction supports Ecad stability and reinforces adhesion. (A)** Ecad planar polarity (enrichment at vertical edges) is shown in *α-Cat-RNAi α-CatX* embryos at stage 8 expressing either GAP43::mCherry or Vinc::mCherry. *n* = number of embryos (e). Significance determined by ordinary two-way ANOVA with uncorrected Fisher's LSD. **(B)** An extra copy of Vinc (Vinc::mCherry) improves adhesion in the ectoderm of *α-Cat-RNAi α-Cat-ΔM23* but not *α-Cat-RNAi α-Cat-ΔM* embryos at stage 8 (live imaged stills shown). Quantification of area of gaps (orange shading) at right. Significance given by Mann-Whitney two-tailed test, *n* = number of embryos (e). **(C and D)** Comparison of control and Vinc-CO embryos expressing Ecad::GFP. Stills from live embryos at stage 8. FI of Ecad and Ecad planar polarity (D) shown, *n* = number of embryos (e). For A, B, and D, bar height represents mean and error bars show SD. **(E)** Denticle belt count of *α-Cat-RNAi α-Cat-ΔM23* embryos with and without a *Vinc* maternal-zygotic (MZ) null mutant background. Number of embryos

analyzed = *n*, significance determined by Chi-square test. **(F)** Live imaged stills comparing Jub::GFP signal in wild-type and a *Vinc* MZ null mutant embryo at stage 8. FI of Jub::GFP in these conditions shown. **(G)** *α-Cat-RNAi α-CatR-ΔM1* embryos at stage 8 show less uniform junctional distribution of Ecad::GFP compared to *α-Cat-RNAi α-CatR* controls as indicated by the increased normalized SD of Ecad::GFP signal at AJs. **(H)** Junctional α-Cat::YFP signal (same color map in F) in stage 8 embryos is reduced and less uniformly distributed in the absence of *Vinc,* as indicated by an increase of the normalized SD of α-Cat::YFP signal. Fluorescent intensity in F and H displayed as in color map shown, maximum intensity (4095), white. For B, C, F, G, and H, scale bar, 10 µm. For C, F, G, and H, bold line shows the median, dotted lines represent interquartile ranges, and *n* = a pooled number of cells (c) or junctions (j) for a number of embryos (e). Mann-Whitney two-tailed test was used to determine significance for C, D, F, G, and H, **** = P < 0.0001, *** = P < 0.001, ** = P < 0.01, * = P < 0.05. **(I)** Schematic summary: Vinc does not play an inhibitory role at AJs. Recruitment of Vinc to the junction depends on M1, and this supports Ecad at higher-tension vertical edges and adhesion. This is in parallel to M2/3, which also supports Ecad recruitment to vertical edges.

tension through a wound-healing response. Laser ablation of the cell cortex to cut the medial actomyosin network initially led to an expansion in cell area and reduction of junctional tension. Subsequently, actomyosin accumulates and contracts, increasing force at junctions of the wounded cell and its neighbors (Yu and Fernandez-Gonzalez 2016; Fig. 8, A–C). Following laser ablation, we measured the responses of Jub and Cno at TCJs of the contracting cell, and the adjacent BCJs in a neighboring cell that are being pulled at. In *α-Cat-RNAi α-CatR* embryos, a consistent peak in Jub intensity was observed following cell contraction—at around 10 min of analysis at BCJs and 3 min at TCJs (Fig. 8, D and E, and Video 9). On average this resulted in a 49 ± 18 and 43 ± 5% increase in Jub intensity at BCJs and TCJs, respectively (Fig. 8, F and G). In *α-Cat-RNAi α-Cat-ΔM* embryos, changes in Jub intensity at both BCJs and TCJs were significantly reduced, especially at BCJs where Jub intensity showed no increase in response to tension (Fig. 8, D–G). Jub signal at TCJs in *α-Cat-RNAi α-Cat-ΔM* embryos also did not reduce in response to cell expansion, when junctional tension is decreased, in contrast to *α-Cat-RNAi α-CatR* controls. Thus, without the M region Jub sensitivity to both increases and decreases in tension is reduced. In *α-Cat-RNAi α-CatR* embryos, bicellular Cno was not impacted by increased tension (Fig. 8, H and J, and Video 10), similar to findings by Yu and Zallen (2020) where Cno at BCJs was unaffected by conditions reducing tension. At TCJs, however, we did observe an increase in Cno intensity by 33 ± 6% following cell contraction (Fig. 8, I and K). Cno intensity in TCJs is already depleted in *α-Cat-RNAi α-Cat-ΔM* embryos, in which we see a smaller increase in Cno intensity at vertices (22 ± 5%, P = 0.054; Fig. 8, I and K). Together, these data further support the conclusion that the M region supports the normal recruitment of Jub and Cno in response to cytoskeletal tension.

The α-Cat M region acts in parallel to Cno to support cell adhesion

Our findings support both α-Cat–dependent and independent mechanisms for Cno junctional recruitment. To further ask whether Cno and α-Cat act in parallel we examined embryos expressing α-Cat M region deletions in a Cno compromised background. Indeed, Cno knockdown enhanced the epithelial defects of all α-Cat deletion constructs (Fig. 9 A). Furthermore, overexpression of Cno improves epithelial integrity in *α-Cat-RNAi*, *α-Cat-RNAi α-Cat-ΔM23*, and *α-Cat-RNAi α-Cat-ΔM* embryos (Fig. 9, B and C). In particular, overexpression of Cno significantly ameliorated the loss of ventral epithelium in *α-Cat-RNAi α-Cat-ΔM23* and *α-Cat-RNAi α-Cat-ΔM* embryos, which are predicted to abolish any binding to Cno, as well as α-Cat-ΔM2 (Fig. 9, C and D). Interestingly, while Cno is significantly depleted at TCJs in *α-Cat-RNAi α-Cat-ΔM23* embryos, Cno overexpression rescues adhesion defects and enhanced tricellular Cno to support adhesion during morphogenesis. Together with the M region–independent association of Cno with AJs, these observations suggest that Cno supports adhesion at TCJs through both a mechanism depending on α-Cat mechanosensing and an α-Cat–independent parallel mechanism. In further support of a parallel pathway we found that knockdown of the Rap1 GTPase, which contributes to Cno membrane recruitment and activation (Sawyer et al., 2011; Bonello et al., 2018; Perez-Vale et al., 2021), enhances the defects in *α-Cat-RNAi α-CatR-ΔM* embryos (Fig. 9 E). During cellularization, Cno recruitment is unaffected by the loss of Arm, and instead requires the small GTPase Rap1 (Sawyer et al., 2009). Our results suggest that Rap1 interaction with Cno shares some parallel function with the M region to support adhesion. These findings suggest that Cno has a role in adhesion that is at least in part redundant to the M region, and to the M1 domain in particular as knockdown of Cno enhances loss of junctional Ecad and cell adhesion defects in α-CatR-ΔM1 embryos compared to α-CatR controls (Fig. 9, A and D).

α-Cat interaction partners and Cno form a cooperative network to support cell adhesion

Given the aforementioned findings, we wondered whether the recruitment of Vinc by M1 is redundant with Cno function. Epithelial integrity was significantly worsened when Vinc is removed from a *cno-RNAi* background, consistent with functional redundancy between Cno and the M1–Vinc interaction (Fig. 9 F). Functional redundancy between Cno and the M1 domain could explain why M1, and similarly, Vinc are dispensable in the embryo. Furthermore, double knockdown of Jub and Cno significantly enhanced adhesion defects compared to Cno knockdown alone (Fig. 9 G). Such findings argue that multiple mechanisms build a robust partially redundant network of interactions to foster AJ stability. Our evidence supports a model where the α-Cat M region itself, and the α-Cat interaction partners Vinc and Jub cooperate with Cno to promote AJ integrity and function (Fig. 9 H).

Discussion

α-Catenin acts as a physical linker between the cadherin/β-catenin complex and the actin cytoskeleton (Desai et al., 2013; Buckley et al., 2014), and through its mechanosensory properties has the potential to modify interactions between cadherins and

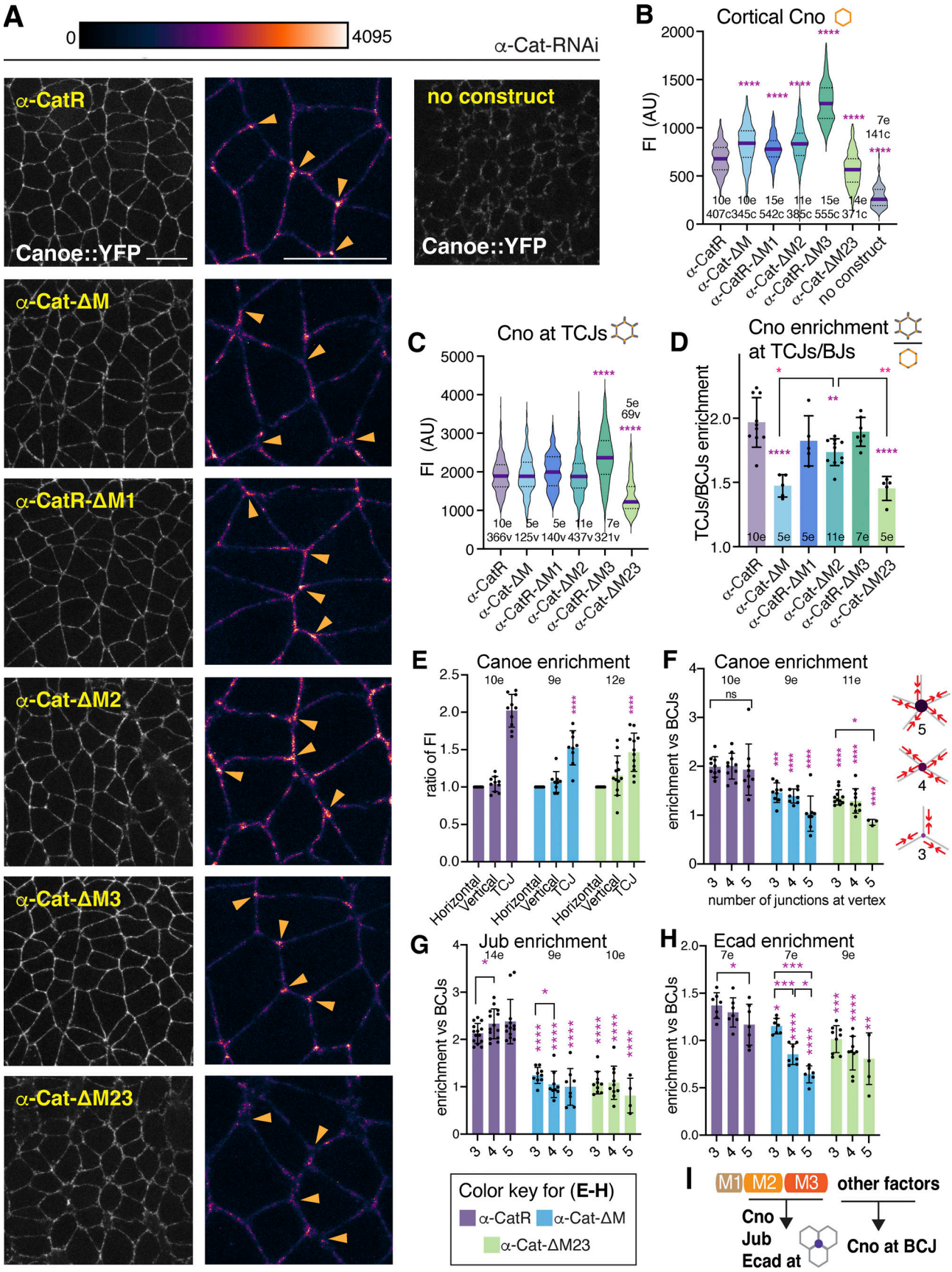

Figure 7. **The α-Cat M region supports the enrichment of Cno at TCJs. (A)** Stills of lateral ectoderm at stage 8 of *α-Cat-RNAi α-CatX* live embryos expressing Cno::YFP. In close-ups at right, orange arrowheads point to TCJs and FI displayed as in color map; maximum FI (4,095), white. Scale bar, 10 µm. **(B)** Cortical

levels of Cno FI in α-*Cat-RNAi α-CatX* embryos. **(C)** Levels of Cno measured at intact TCJs in α-*Cat-RNAi α-CatX* embryos. For B and C, significance is determined by Kruskal–Wallis test with Dunn's multiple comparisons test; bold line, median; dotted lines, interquartile ranges; and *n* = a pooled number of cells (c) or vertices (v) for a number of embryos (e). **(D)** Ratio of the mean FI Cno at TCJs vs. BCJs is plotted per embryo. Significance is given by ordinary one-way ANOVA with Tukey's multiple comparisons test. **(E)** Ratio of mean Cno FI in horizontal and vertical BCJs and TCJs per embryo. Significance determined by ordinary two-way ANOVA with Tukey's multiple comparisons test. **(F–H)** Ratio of mean FI of Cno (F), Jub (G), and Ecad (H) at vertices joining three, four, or five cell junctions as compared to mean FI at BCJs within the same embryo (schematic at right; red arrows indicate contractile actomyosin). For plots in D–H, bar height represents mean, error bars represent SD, and *n* = number of embryos analyzed (e). For E–H, significance determined by ordinary two-way ANOVA with Tukey's multiple comparisons test. Comparisons between vertices linking three, four, and five junctions performed as pairwise within embryos by using two-way ANOVA as a mixed effects model with Geisser-Greenhouse correction and Tukey's multiple comparisons test (**** = P < 0.0001, *** = P < 0.001, ** = P < 0.01, * = P < 0.05). **(I)** Schematic summary: While Cno is recruited to BCJs through an alternate pathway, M2/3 supports the enrichment of a pool of Cno at vertices, as well as enrichment of Jub and Ecad.

the cytoskeleton in response to external or internal forces (Yonemura et al., 2010; le Duc et al., 2010; Borghi et al., 2012). Two mechanosensory regions within α-catenin have been identified: the C-terminal actin-binding domain of α-catenin increases binding strength to F-actin as force is applied (Buckley et al., 2014; Ishiyama et al., 2018; Xu et al., 2020; Wang et al., 2022), and the central M region of α-catenin that acts principally by modifying interactions between α-catenin and interaction partners in response to force (Yonemura et al., 2010; Ishiyama et al., 2013; Thomas et al., 2013; Yao et al., 2014; Li et al., 2015; Maki et al., 2016; Seddiki et al., 2018; Barrick et al., 2018; Matsuzawa et al., 2018; Terekhova et al., 2019; Sarpal et al., 2019; Alégot et al., 2019; Boutillon et al., 2022). How α-catenin mechanosensing cooperates with multiple interaction partners that can also bind to F-actin to dynamically adjust adhesion during morphogenesis has remained largely unexamined.

We determined that the M region of *Drosophila* α-Cat plays a key role in maintaining cell adhesion during active junctional remodeling that drives morphogenesis in the early embryo. Taking advantage of the well-described tension landscape in the ectoderm as it undergoes cell intercalation during germband extension (Bertet et al., 2004; Fernandez-Gonzalez et al., 2009; Tetley et al., 2016), we determined that the M region supports the junctional recruitment of Vinc, Jub, and Cno in response to cytoskeletal tension, which function redundantly to support adhesion. While direct physical interaction between *Drosophila* α-Cat and Vinc, Jub, or Cno have not been reported, our data and work of others (Alégot et al., 2019) suggest that recruitment of Vinc and Jub to AJs critically depends on direct or indirect interaction between Vinc and the M1 domain and Jub and the N2 domain of α-Cat. In contrast, Cno localizes at AJs through mechanisms that are independent of α-Cat and supports cell adhesion in a parallel pathway. Only the mechanosensitive enrichment of Cno at TCJs (Yu and Zallen, 2020) requires its interaction with the M2 and M3 domains of α-Cat.

Characterization of the M region in both mammalian αE-catenin and *C. elegans* HMP1 by single molecule manipulation suggest that unfolding of M region domains occurs within physiological ranges of force (<20 pN) in a stepwise manner (Yao et al., 2014; Maki et al., 2016; Le et al., 2021 *Preprint*). Without force, the M region of α-catenin is stabilized in a closed conformation by a dynamic network of salt-bridges, which is largely conserved in *Drosophila* (Ishiyama et al., 2013; Li et al., 2015). Under application of force (5 pN αE-catenin, 10–15 pN HMP1), M1 is unfurled, allowing the binding of Vinc (Yao et al., 2014; Maki et al., 2016; Le et al., 2021 *Preprint*). This force activated Vinc binding is conserved even in the more distantly related HMP1 (Le et al., 2021 *Preprint*). Next, at a higher range of forces (10–15 pN αE-catenin, 15–20 pN HMP1), a further conformational change, likely affecting the M2 and M3 domains takes place (Yao et al., 2014; Le et al., 2021 *Preprint*). Moreover, a higher fraction of molecules in an open conformation found at vertices/TCJs that could be further enhanced through the application of force has been reported for αE-catenin (Yonemura et al., 2010). Projecting these findings onto our results, we propose a model where the frequency of three different tension states of α-Cat may correspond to the differential junctional recruitment (through direct or indirect binding) of interaction partners (Fig. 10). (i) Moderate amounts of Vinc and Jub are recruited to AJs at low-tension BCJs (=horizontal junctions in the extending germband). (ii) At medium-tension BCJs (=vertical junctions in the extending germband), recruitment of Vinc and Jub is significantly increased. We suggest this difference between horizontal and vertical edges could be explained by a higher range of forces at the vertical edge, which allow more α-Cat molecules to adopt an unfurled M1 conformation, facilitating both Vinc binding to M1 and Jub recruitment by N2. In contrast, at horizontal edges, which are under lower tension, a smaller fraction of α-Cat molecules may be found in the unfurled M1 conformation. (iii) Finally, at TCJs, which experience the highest levels of tension, Vinc and Jub are further elevated, and Cno is enriched in response to α-Cat mechanosensing. Here, the highest range of forces may lead to the highest fraction of α-Cat molecules with unfolded M2 and\or M3, allowing α-Cat to engage not only high levels of Vinc and Jub but also to interact with Cno to further stabilize AJs (Fig. 10, A–C).

The M1, M2, and M3 domains of α-Cat make distinct contributions to cell adhesion. M2 has a major role in supporting surface stability of the CCC and is required for the mechanosensitive AJ enrichment of Jub, which further stabilizes the junction. Together with M3, M2 supports Cno recruitment to TCJs to further reinforce AJs (Fig. 10 A). Recently, mechanical coupling between the M2 and N2 domains has been proposed (Terekhova et al., 2019), as well as direct, transient interaction between the disordered N-terminal region of β-catenin and the M region (Bush et al., 2019), suggesting that M2 could participate in strengthening interactions at the N-terminal domain with Jub and Arm. In embryos lacking M2, cortical levels of both Jub and Vinc, as well as Cno enrichment at TCJs, are reduced.

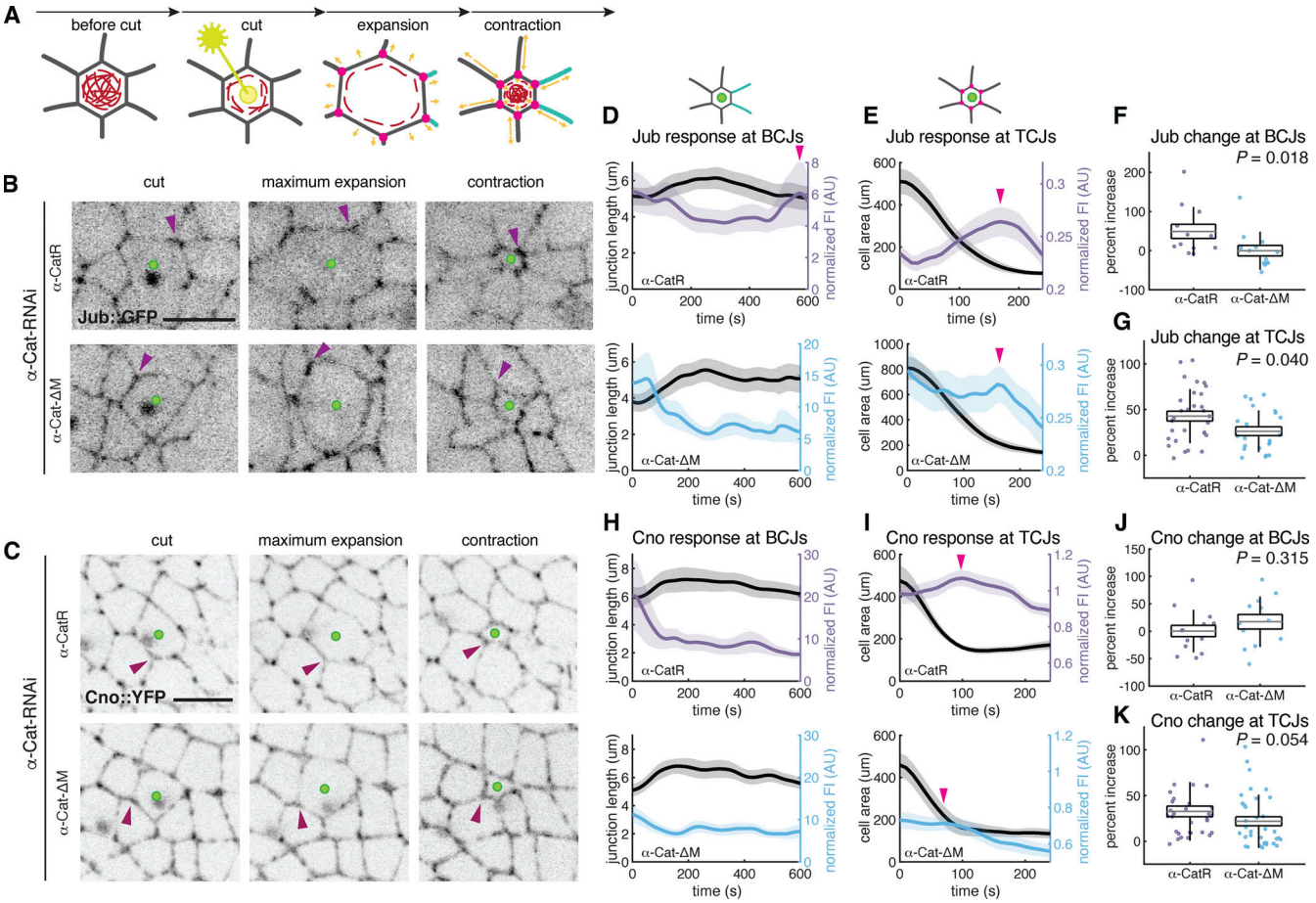

Figure 8. **The α-Cat M region supports the mechanosensitive recruitment of Jub and Cno. (A)** Schematic illustrating protocol for laser ablation experiment to ectopically change tension. Red, actomyosin; pink, TCJs analyzed; cyan, BCJs analyzed; yellow, cytoskeletal force. **(B and C)** Stills from movie of *α-Cat-RNAi α-CatX* embryos analyzed, expressing Jub::GFP (B) or Cno::YFP (C). Green spot marks laser cut cell. Arrowhead highlights a TCJ. Scale bar,10 µm. **(D)** FI of Jub::GFP in BCJs pulled by cut cell after laser ablation. For *α-Cat-RNAi α-CatR*, *n* = 14 junctions measured from 7 embryos; *α-Cat-RNAi α-Cat-ΔM*, *n* = 14 junctions measured from 7 embryos. **(E)** FI of Jub::GFP in TCJs of cut cell following laser ablation. For *α-Cat-RNAi α-CatR*, *n* = 14 junctions measured from 7 embryos; *α-Cat-RNAi α-Cat-ΔM*, *n* = 12 junctions measured from 6 embryos. **(F and J)** Change in FI at BCJs for Jub::GFP (F) and Cno::YFP (J) in response to increase in tension. Per junction, maximum peak of FI at 10 min of analysis is plotted as a percent increase from minimum in FI at time point of greatest junction length. **(G and K)** Change in FI at TCJs for Jub::GFP (G) and Cno::YFP (K) in response to increase in tension. Per junction, maximum peak in FI within 4 min of contraction is plotted as a percent increase from minimum in FI in 1 min following maximum cell expansion. **(H)** FI of Cno::YFP in BCJs pulled by cut cell after laser ablation. For *α-Cat-RNAi α-CatR*, *n* = 31 junctions measured from 7 embryos; *α-Cat-RNAi α-Cat-ΔM*, *n* = 22 junctions measured from 6 embryos. **(I)** FI of Cno::YFP in TCJs of cut cell following laser ablation. For *α-Cat-RNAi α-CatR*, *n* = 31 junctions measured from 7 embryos; *α-Cat-RNAi α-Cat-ΔM*, *n* = 35 junctions measured from 8 embryos. For D, E, H, and I, FI is normalized to correct for photobleaching, curves are aligned by time point of maximum expansion, and smoothed traces are plotted, representing mean and SEM for all junctions analyzed. Pink arrowhead marks peaks in smoothened mean signal. For F, G, J, and K, P values are given by Mann–Whitney tests; gray line, mean, box, SEM, whiskers, SD.

Effects on multiple interaction partners at once could explain the strong adhesion defects observed in these embryos.

The M2/3 and M1 domains appear to have opposing roles in both adhesion and regulation of tissue growth (this work, Sarpal et al., 2019). M1 is required for growth regulation, and dispensable for adhesion, while the opposite is largely true for the M2 and M3 domains. This suggests that M region mechanosensing acts similarly in cell adhesion and tissue growth and that the tissue-specific consequences are due to differences in downstream pathways that impact on growth versus adhesion. Contrary to current models, we find that M1 negatively regulates CCC-dependent adhesion through inhibition of Jub recruitment, which may be released by M1 unfurling in response to force. While M1 recruitment of Vinc supports AJs stability, this contribution is subtle and dispensable for both adhesion and growth (Sarpal et al., 2019, this work). This is consistent with dispensability for the α-catenin Vinc binding domain and Vinc for barrier function in zebrafish (Han et al., 2016) and worsening of the zygotic *α-Cat* mutant phenotype by combination with a *Vinc* mutation (Jurado et al., 2016). M region mechanosensing and Vinc were recently implicated in coordinating the migration of non-epithelial Polster cells in the zebrafish gastrula (Boutillon et al., 2022). In *Drosophila*, we noticed that the loss of M1 or Vinc let to a somewhat enhanced clustering of the CCC, suggesting that the M1–Vinc interaction supports the uniform distribution of the CCC at cell contacts. Genetic analysis suggests that the M1–Vinc interaction is redundant with Cno and that Cno and the M region act in parallel to support AJs. Additional α-Cat

Figure 9. **Cno supports Ecad stability in a parallel pathway to the α-Cat M region. (A)** Quantification of cuticle defects from *cno-RNAi α-Cat-RNAi α-CatX* and *gfp-RNAi α-Cat-RNAi α-CatX* embryos. Phenotypic categories are color-coded and examples are given in Fig. S5. **(B)** Overexpression of Cno improves

epithelial integrity in *α-Cat-RNAi* embryos. **(C)** Denticle belt count for *α-Cat-RNAi α-CatX* embryos overexpressing Cno or *GFP-RNAi* as control. *gfp-RNAi* controls same as in Fig. 5 E. **(D)** Ectoderm at stage 8/9 of *α-Cat-RNAi α-CatX* embryos immunostained for Ecad, expressing either *UAS-cno*, *cno-RNAi* or *UAS-gfp-RNAi* as control. Ecad levels are enhanced by Cno overexpression, ameliorating defects found in α-Cat-ΔM23 embryos, whereas Cno knockdown causes an enhancement of AJ fragmentation in α-CatR-ΔM1 embryos compared to control. Scale bar, 10 µm. **(E)** *Rap1-RNAi* enhances defects in *α-Cat-RNAi α-CatR* and *α-Cat-RNAi α-Cat-ΔM* embryos. *gFP-RNAi* controls same as in C. Chi-square test, **** = P < 0.0001. **(F)** *Vinc* null mutant enhances defects caused by *cno-RNAi*. Chi-square test, **** = P < 0.0001. **(G)** *jub-RNAi* enhances defects caused by *cno-RNAi*. Chi-square test, *** = P < 0.001. For A–C and E–G, *n* = number of embryos analyzed. **(H)** Schematic summary: Redundancy between the M region interactors Jub, Vinc, and Cno support epithelial integrity. Cno supports adhesion in part through M2/3-dependent recruitment to TCJs and an α-Cat independent pathway involving Rap1. Arrows denote functional relationships.

M region interaction partners such as α-Actinin (Nieset et al., 1997) or srGAP (Serre et al., 2022) remain to be investigated in our system, and could contribute to the redundant, multivalent interactions at the CCC–actin interface.

Recent analysis of Cno function in the *Drosophila* ectoderm highlighted the need for multiple, partially redundant interactions between Cno, the plasma membrane, and the cytoskeleton in support of AJ stability during tissue morphogenesis (Manning et al., 2019; Perez-Vale et al., 2021). Thus, both Cno and α-Cat stabilize AJs through multiple interactions. It is unclear, however, whether Cno is a mechanosensor or only responds to mechanosensory inputs by α-Cat as we show here or by other mechanisms as Cno enrichment at TCJs is also enhanced by phosphorylation of Cno by the Abl non-receptor tyrosine kinase (Yu and Zallen, 2020). Whether phosphorylation of Cno modifies the interactions with α-Cat remains to be explored. Cno at TCJs needs to be dynamic to enable normal vertex resolution during the cell rearrangements required for cell intercalation (Yu and Zallen, 2020).

Taken together, our work suggests that the α-Cat M region acts in cell adhesion to support embryonic morphogenesis through mechanosensitive modulation of interactions with Vinc, Jub, and Cno. The M1–Vinc interaction, dispensable on its own, shows redundancy with Cno function. While Vinc and Jub association with AJs is completely dependent on α-Cat mechanosensing, the association of Cno with AJs depend on α-Cat mechanosensing only for its enrichment at TCJs. Cno supports

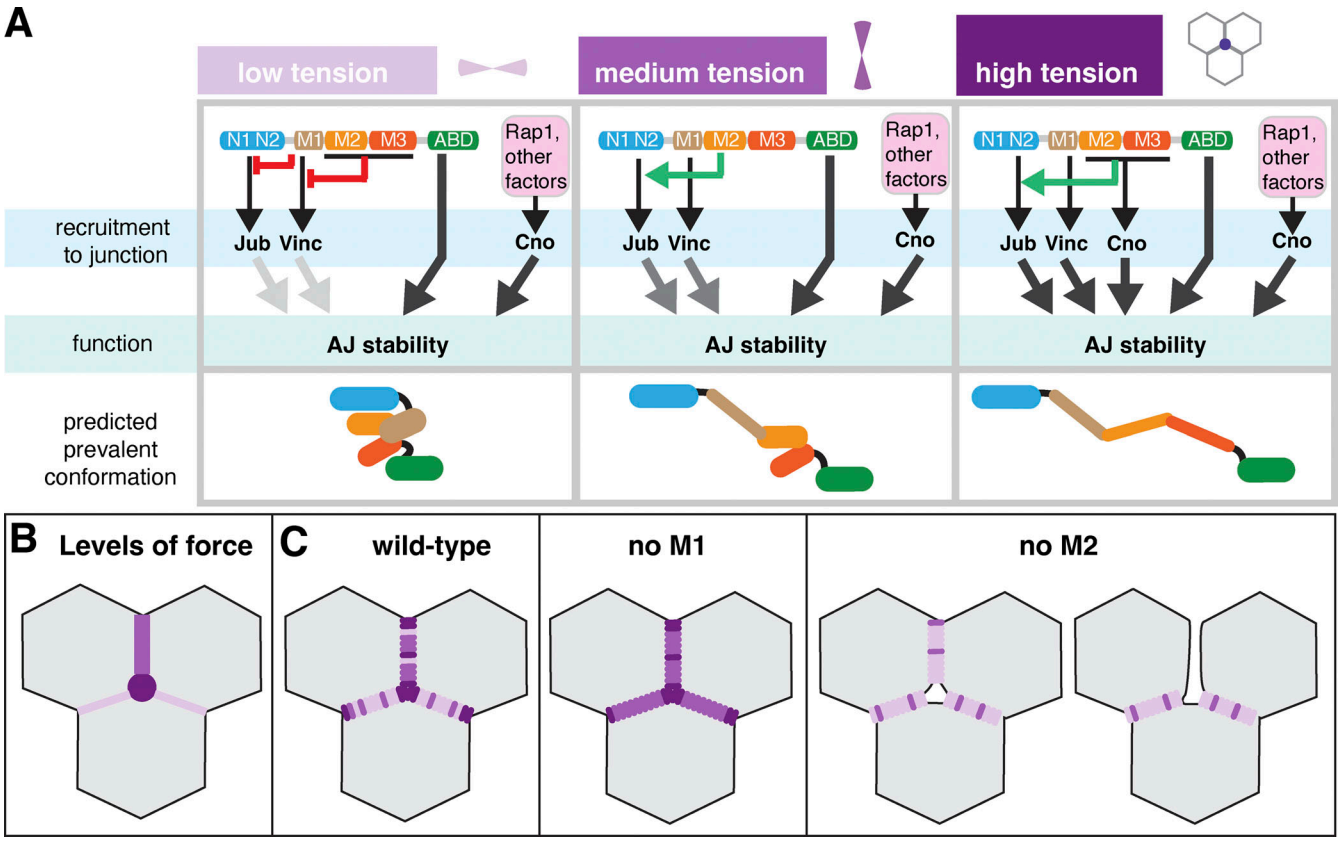

Figure 10. **Model of α-Cat M region mechanosensing in the *Drosophila* ectoderm during germband extension. (A)** Schematic summarizing the distinct contributions of α-Cat M region domains to the membrane recruitment of interaction partners at low-, medium-, and high-tension cell contacts. Arrows indicate functional relationships; models of predicted corresponding M region conformations illustrated at bottom. M region domains have an inhibitory effect on each other. Cno acts in parallel with the M region and M region interactors to support AJ stability. **(B)** Diagram illustrating the tension landscape in the ectoderm during germband extension, showing low-tension contacts (horizontal edges), medium-tension contacts (vertical edges), and high-tension contacts (TCJs/vertices). **(C)** Schematic illustration of anticipated distribution of the three α-Cat conformations highlighted in A in wild-type, α-*Cat-RNAi α-CatR-ΔM1* embryos, and α-*Cat-RNAi α-Cat-ΔM2*. See text for further discussion.

adhesion at bicellular contacts in a parallel pathway to α-Cat. We suggest that these redundant and cooperative multivalent interactions are the molecular basis of the mechanoresponsive dynamic stabilization of AJs that maintain tissue integrity as the epithelium undergoes cell contacts changes.

Materials and methods

Drosophila genetics

Flies were raised on standard media at 25°C for all experiments. For rescue experiments, males carrying *mat-GAL4* (*P{matα4-GAL-VP16}67*; Häcker and Perrimon, 1998) and the α-Cat constructs (inserted at *attP2*) were crossed to females carrying fluorescently tagged proteins of interest and *UAS-α-Cat-RNAi* (TRiP HMS00317, Transgenic RNAi project [TRiP]). F1 virgin females carrying *mat-GAL4*, fluorescent protein, and α-Cat construct were then crossed to OregonR wild-type males (except *jub::GFP* males were used for rescue experiments measuring Jub::GFP) and the progeny of this cross were analyzed. Similarly, for double knockdown analysis, F1 virgin females carrying both *mat-GAL4* and transgenes were crossed to OregonR wild-type males and their progeny assessed. In *Vinc* mutant analysis, a complete genomic deletion of *Vinc*, $Vinc^{102.1}$ was used (Klapholz et al., 2015). See Table S1 for details of crosses used for each figure. The following fly lines were employed:

UAS constructs

α-CatR, *α-CatR-ΔM1*, *α-Cat-ΔM* (aka: *α-CatR-ΔM*), *α-CatR-ΔM3* (Sarpal et al., 2019); *α-Cat-ΔM2* (aka: *αCatΔVH2-N*), *α-Cat-ΔM23* (aka: *αCatΔVH2*), *DE-cadΔβ::α-CatABD* (aka: *DE-cadΔβ::VH3-CTD*); *UAS-GFP* (Desai et al., 2013); *Vinc-CO* (Maartens et al. 2016); *UAS-Cno* (aka: *CanoeFL::GFP*; Bonello et al., 2018).

RNAi lines

α-Cat-RNAi (TRiP HMS00317); *jub-RNAi* (TRiP HMS00714); *canoe-RNAi* (TRiP HMS00239 and GL00633); *Rap1-RNAi* (TRiP HMJ21898) were produced by the TRiP at Harvard (Zirin et al., 2020). *GFP-RNAi* (BL41552, BDSC) and *Ed-RNAi* (v938, VDRC) were soured from the Bloomington *Drosophila* Stock Center (BDSC) and the Vienna *Drosophila* Resource Center (VDRC).

Fluorescently tagged markers

α-Cat::YFP (α-CatCPTI002516), *Canoe::YFP* (cnoCPTI000590), and *Zipper::YFP* (zipCC01626) are derived from the Cambridge Protein Trap Insertion project, Kyoto Stock Centre (Lye et al., 2014; Lowe et al., 2014). Other fluorescently tagged proteins are insertions under the control of the respective endogenous promoter: Ecad::GFP (aka: DEcad::GFP, *shg>DEcad::GFP*; Huang et al., 2009); Vinc::mCherry (recombined with Ecad::GFP; Kale et al., 2018); Jub::GFP (Sabino et al., 2011). Fluorescently tagged proteins ubiquitously expressed in the early embryo: Ani-RBD (aka: *ubi>Anillin-RBD::GFP*; Munjal et al., 2015) and *sqh>GAP43::mCherry* (Martin et al., 2010).

Preparation of cuticle and quantification of embryonic lethality

To analyze the terminal cuticle phenotype of embryos, eggs collected overnight at 25°C were aged for 2 d or 24 h if viable, and then washed in water and dechorionated for 5 min in 2.15% sodium hypochlorite. After a second wash, embryos were mounted on a slide into a 3:2 mixture of Hoyer's medium and lactic acid and incubated at 85°C overnight. To determine the percentage of embryonic lethality, flies were allowed to lay eggs at 25°C for an 8-h period, and between 100 and 300 eggs were counted and arranged into rows on a new agar plate. This plate was then examined 24 and 48 h later to count hatched larvae and dead embryos.

Antibody staining

Drosophila embryos were dechorionated in 2.15% sodium hypochlorite and then either heat-fixed in a salt solution (Miller et al., 1989; Figs. 9 and S4) or fixed for 20 min in 4% formaldehyde in a 1:1 PBS:heptane mixture (Fig. S2). Primary antibodies used under heat fixation were anti-HA (rat monoclonal, 3F10; 1:500; Roche), anti-Cno (rabbit 1:1,000, a gift from Mark Peifer, University of North Carolina, Chapel Hill, NC, USA), anti-DE-cadherin (rat monoclonal DCAD2 1:25; Developmental Studies Hybridoma Bank). Under heptane fixation: anti-HA (mouse 16B12 1:100; Abcam). For immunostaining in Fig. S1, ovaries were fixed in 5% formaldehyde in phosphate buffer for 10–12 min. Primary antibodies used for immunostaining were: anti-HA (rat monoclonal 3F10, 1:600; Roche); anti-Arm (mouse monoclonal N2 7A1, 1:100; DSHB); anti-α-spectrin (rabbit polyclonal, 1:1,000, gift from Daniel Branton, Harvard University, Cambridge, MA, USA); anti-GFP (mouse monoclonal JL-8, 1:400; Clontech). Secondary antibodies were used at a concentration of 1:400 (Invitrogen).

Analysis in follicular epithelium

A heat-shock inducible MARCM system was employed as previously described (Sarpal et al., 2012; Desai et al., 2013). For cell clones produced in the follicular epithelium, the percentage of rescued cells was calculated. The following recombinant lines were used for MARCM analysis: *hs–Flp FRT40A; da–Gal4 UAS–mCD8::GFP α-Cat*^{1}*/TM6B*; *tub–Gal80 ubi–α-Cat FRT40A; act–Gal4 α-CatX α-Cat*^{1}*/TM6B* (Sarpal et al., 2012; Desai et al., 2013; Sarpal et al., 2019).

Imaging and signal intensity quantification

Live imaging was performed on dechorionated embryos mounted in Halocarbon Oil 27 (Sigma-Aldrich) between an oxygen permeable membrane (YSI; Xylem Inc.) and coverslip, and short time-lapse movies were acquired, similar to other previously described methods (Blankenship et al., 2006). Imaging was performed at room temperature using a Leica TCS SP8 scanning confocal microscope with 40× or 63× objectives (HC PL APO CS2 with NAs of 1.30 and 1.40, respectively) and using Leica LASX Software (Leica Microsystems). A Carl Zeiss Axiophot2 microscope using a phase-contrast 20× lens (NA 0.5) connected to a Canon Rebel XSi camera was used to capture images of embryonic cuticles, and time-lapse movies were captured using this scope and a 10× lens (NA 0.14) to determine rates of germband extension. The number of embryos per genotype is listed on each figure.

Z-stacks were collected using a z-step size of 0.35–0.4 μm, starting from above the vitelline membrane and moving well

through all visible apical junctional structures for 15–20 steps. Planes containing autofluorescence of the vitelline membrane were removed in post-processing and maximum projections were produced using Fiji (Schindelin et al., 2012). All images shown are such maximum projections unless otherwise indicated. GAP43::mCherry signal in supplemental videos is displayed as a median projection of three z-slices. Adobe Illustrator was used to assemble confocal images. Curves were adjusted in Adobe Photoshop for Vinc::mCherry confocal images (Fig. 4), antibody staining of Ecad (Fig. 9), and images of cuticle preparations, and this was performed equally across conditions within the same experiment. For images shown using a colormap legend, the "gem" lookup table in Fiji was used. The same settings on confocal equipment and image processing were applied for all images within the same experiment.

Analysis of early embryonic phenotypes and germband extension

α-Cat-RNAi α-CatX expressing embryos were live imaged during stages 6, 7, and 8 and phenotypic categories were determined for embryos within a Jub::GFP, Ecad::GFP, GAP43::mCherry, or myosin::YFP background. For quantification of germband extension, the change in position of the proctodeal invagination after 40 min was normalized to the total length of the embryo.

Fluorescent intensity

Analysis of cortical levels of fluorescence was performed using the Matlab script SIESTA (scientific image segmentation and analysis; Fernandez-Gonzalez and Zallen, 2011). For a number of embryos, a polyline 3 pixels in width was drawn along the perimeter of each cell, and the mean FI along this line, minus the mean FI within the center of the cell, was plotted as cortical FI. Total junctional myosin is given as the sum of the mean fluorescence along the perimeter and mean fluorescence within the perimeter for each cell (total FI). Junctional/total myosin fraction is given as the average FI of myosin at the cell perimeter (junctional) out of total myosin (fraction of total FI). For comparison of Ani-RBD at the edge of gaps versus cells not in contact with a gap, the average FI along the perimeter (perimeter FI) was plotted for polylines drawn along cells (intact) versus along the gap (gap).

Planar polarity

Using SIESTA, trajectories 3 pixels in width were drawn along individual cell edges, avoiding overlap or vertices, and these edges were grouped into 15° bins, reflected about the DV axis. For each bin, the cytoplasmic fluorescence of the image was subtracted from the average FI of cell edges. This value was then divided by that of the 0–15 (horizontal) bin. Enrichment to vertical edges is plotted from this calculation for the 75–90° bin. To show the FI of Jub or Ecad at vertical or horizontal edges, for each embryo cytoplasmic fluorescence is subtracted from the average FI of edges in the vertical (75–90°) and the horizontal (0–15°) bins.

Analysis of vertices

Fluorescence within cell vertices was measured using the ellipse tool in Fiji for 30–45 vertices per embryo. For enrichment at vertices, the mean intensity of vertices was divided by the mean intensity of bicellular cell edges per embryo. Bicellular cell junctions were measured through trajectories drawn in SIESTA, or lines drawn in Fiji.

Quantification of gaps

In Fiji, on an image representing a field of view of 2,136.4 μm^2, the brush tool was used to mask each gap, and then the wand tool was used to measure area of gap and fit ellipse.

Colocalization of signal

To determine the degree of colocalization of Cno versus α-Cat construct signal, regions of interest of junctions were compared for a number of embryos using the coloc2 plugin in ImageJ.

Laser ablation analysis

Live embryos were prepared as described above and imaged using a Revolution XD spinning-disk confocal microscope equipped with an iXon Ultra 897 camera (Andor), a 60x oil immersion lens (NA 1.35; Olympus), and MetaMorph Software (Molecular Devices). 16-bit Z-stacks were acquired at 0.5 μm steps every 10s (20 slices per stack) for 15 min, and maximum intensity projections were used for analysis. Jub::GFP was illuminated using a 488 laser with 30% intensity and 100 gain. Cut cells were selected based on position and stage (ventral ectoderm, stage 7), and were centered within the field of view. A pulsed Micropoint N2 laser (Andor) tuned to 365 nm, with an attenuation plate setting of 20, was applied to the cell cortex for 10 pulses. Image analysis was performed using PYJAMAS (Fernandez-Gonzalez et al., 2021). In order to segment cells, polylines were drawn using the Livewire function for each cell/frame individually. TCJs were segmented by placing fiducials at each junction. Background intensity was removed by subtracting the mode of the image and photobleaching correction was performed by dividing by the mean pixel intensity of the frame. Pixel width for analysis was 3 pixels. Cell outlines were used to calculate cell area at each time point. Cell area and vertex intensity traces over time were smoothed using a Gaussian filter with a width of 1 min (six time points). Since wounded cells expanded prior to rapidly contracting, the maximum cell area was identified as the start of cell contraction and cell area was tracked for the next 4 min at the end of which cell area had stabilized. To measure the change in tricellular vertex intensity in response to the change in cell area, we compared the minimum vertex intensity in the 1 min after maximum area to the maximum intensity reached by the vertex in the 4 min following initiation of cell contraction. To measure the change in bicellular junction intensity in the cell neighboring the contracting cell, we compared the minimum junction intensity at the time the junction fully extended to the maximum intensity at the junction 10 min later.

Statistics

Prism v9 (GraphPad) was used for statistical analysis and plots, except for the balloon plot in Fig. 4, which was made using Microsoft Excel, and plots in Fig. 8, which were generated using MATLAB. In violin plots, bold lines indicate the median, thinner

lines represent interquartile ranges. For bar graphs, height of bar indicates mean, and error bars indicate SD (except Fig. S1, error bars give SEM). In box-and-whisker plots (Fig. 8), gray line indicates the mean, edges of box mark SEM, and whiskers represent SD. Significance was calculated on measurements from each cell, junction, or vertex for a number of embryos, denoted on each plot. In experiments with only two conditions, the Mann-Whitney unpaired two-tailed *t* test was used. When comparing more than two conditions, and output consisted of single measurements per *n*, ordinary one-way ANOVA with Tukey's multiple comparisons test was used unless distribution was non-normal, where Kruskal–Wallis test with Dunn's multiple comparisons test was used to determine significance. Normality was assessed using D'Agostino & Pearson test, Shapiro-Wilk test and normal QQ plot. To compare enrichment of AJ proteins at bicellular junctions within the same bin of cell edge trajectories under multiple conditions, ordinary two-way ANOVA with uncorrected Fisher's Least Significant Difference (LSD) was performed. Two-way ANOVA used to determine significance when comparing enrichment of AJ proteins in vertices joining three, four, or five junctions, with Tukey's multiple comparisons test to compare across conditions, and a mixed effects model with Geisser-Greenhouse correction and Tukey's multiple comparison test on vertices within the same embryo. To compare terminal cuticle phenotypes, Chi-square analysis was performed on pairs of conditions.

Online supplemental material

Fig. S1 shows the analysis of α-Cat-ΔM within ovarian follicular epithelium. Fig. S2 shows additional data on the effectiveness of knockdown by *α-Cat-RNAi*, cellular distribution of constructs, and examples of cuticle phenotypes. Fig. S3 provides a detailed breakdown of the analysis of FI of Ecad, Vinc, Jub, and Cno by edge angle or vertex type. Fig. S4 shows data illustrating the relationship between α-Cat and Cno. Fig. S5 demonstrates the phenotypic categories used to score cuticle defects and contains a legend for graphics used in figures. Table S1 contains a summary of genotypes used and breakpoints of constructs used. Video 1 shows a gastrulating embryo expressing *α-Cat-RNAi*. Videos 2, 3, 4, 5, 6, 7, and 8 show examples of gastrulation in embryos expressing *α-Cat-RNAi* and M region deletion constructs. The constructs expressed in these embryos are as follows: Video 2: α-CatR; Video 3: α-Cat-ΔM (an embryo with strong defects); Video 4: α-Cat-ΔM (an embryo with moderate defects); Video 5: α-CatR-ΔM1; Video 6: α-Cat-ΔM23; Video 7: α-CatR-ΔM3 (an embryo with stronger defects); and Video 8: α-Cat-ΔM2. Video 9 shows examples of movies analyzed in the laser ablation experiment to measure Jub mechanosensitive recruitment, and examples of movies analyzed to investigate Cno mechanosensitive recruitment are shown in Video 10.

Data availability

All data are available in the manuscript or supplementary materials. Transgenic *Drosophila* stocks from Desai et al. (2013) or Sarpal et al. (2019) are available upon request.

Acknowledgments

We thank Ritu Sarpal and Limin Wang for providing the data shown in Fig. S1. We thank Mark Peifer for discussion of unpublished data and comments on the manuscript. We thank Dorothea Godt for critical reading of the manuscript. We thank Nick Brown, Thomas Lecuit, Mark Peifer, the BDSC, the *Drosophila* RNAi Screening Center at Harvard Medical School, and the Developmental Studies Hybridoma Bank for reagents. We like to thank the Imaging Facility of the Department of Cell and Systems Biology, University of Toronto, for support.

This work was funded by a project grant from the Canadian Institutes of Health Research (CIHR; to U. Tepass). R. Fernandez-Gonzalez is the Canada Research Chair in Quantitative Cell Biology and Morphogenesis. U. Tepass is a Canada Research Chair for Epithelial Polarity and Development. K.E. Rothenberg was supported by a postdoctoral fellowship from the CIHR, and by a grant from the CIHR to R. Fernandez-Gonzalez.

Author contributions: The project was conceived and experiments were designed by L. Sheppard and U. Tepass. L. Sheppard carried out experiments and data analysis. Laser ablation experiments were performed and analyzed by D.G. Green and G. Lerchbaumer, with formal analysis performed by K.E. Rothenberg, under the supervision of R. Fernandez-Gonzalez. U. Tepass provided supervision and raised funds. The paper was written by L. Sheppard and U. Tepass.

Disclosures: The authors declare no competing financial interests.

Submitted: 17 August 2021
Revised: 8 September 2022
Accepted: 18 November 2022

References

Abreu-Blanco, M.T., J.M. Verboon, and S.M. Parkhurst. 2014. Coordination of Rho family GTPase activities to orchestrate cytoskeleton responses during cell wound repair. *Curr. Biol.* 24:144–155. https://doi.org/10.1016/j.cub.2013.11.048

Alatortsev, V.E., I.A. Kramerova, M.V. Frolov, S.A. Lavrov, and E.D. Westphal. 1997. Vinculin gene is non-essential in Drosophila melanogaster. *FEBS Lett.* 413:197–201. https://doi.org/10.1016/s0014-5793(97)00901-0

Alégot, H., C. Markosian, C. Rauskolb, J. Yang, E. Kirichenko, Y.C. Wang, and K.D. Irvine. 2019. Recruitment of Jub by α-catenin promotes Yki activity and Drosophila wing growth. *J. Cell Sci.* 132:jcs222018. https://doi.org/10.1242/jcs.222018

An, Y., G. Xue, Y. Shaobo, D. Mingxi, X. Zhou, W. Yu, T. Ishibashi, L. Zhang, and Y. Yan. 2017. Apical constriction is driven by a pulsatile apical myosin network in delaminating Drosophila neuroblasts. *Development.* 144:2153–2164. https://doi.org/10.1242/dev.150763

Angulo-Urarte, A., T. van der Wal, and S. Huveneers. 2020. Cell-cell junctions as sensors and transducers of mechanical forces. *Biochim. Biophys. Acta Biomembr.* 1862:183316. https://doi.org/10.1016/j.bbamem.2020.183316

Barrick, S., J. Li, X. Kong, A. Ray, E. Tajkhorshid, and D. Leckband. 2018. Salt bridges gate α-catenin activation at intercellular junctions. *Mol. Biol. Cell.* 29:111–122. https://doi.org/10.1091/mbc.E17-03-0168

Barry, A.K., H. Tabdili, I. Muhamed, J. Wu, N. Shashikanth, G.A. Gomez, A.S. Yap, C.J. Gottardi, J. de Rooij, N. Wang, and D.E. Leckband. 2014. α-catenin cytomechanics--role in cadherin-dependent adhesion and mechanotransduction. *J. Cell Sci.* 127:1779–1791. https://doi.org/10.1242/jcs.139014

Barstead, R.J., and R.H. Waterston. 1991. Vinculin is essential for muscle function in the nematode. *J. Cell Biol.* 114:715–724. https://doi.org/10.1083/jcb.114.4.715

Bertet, C., L. Sulak, and T. Lecuit. 2004. Myosin-dependent junction remodelling controls planar cell intercalation and axis elongation. *Nature*. 429:667–671. https://doi.org/10.1038/nature02590

Blankenship, J.T., S.T. Backovic, J.S.P. Sanny, O. Weitz, and J.A. Zallen. 2006. Multicellular rosette formation links planar cell polarity to tissue morphogenesis. *Dev. Cell*. 11:459–470. https://doi.org/10.1016/j.devcel.2006.09.007

Boettner, B., P. Harjes, S. Ishimaru, M. Heke, H.Q. Fan, Y. Qin, L. Van Aelst, and U. Gaul. 2003. The AF-6 homolog canoe acts as a Rap1 effector during dorsal closure of the Drosophila embryo. *Genetics*. 165:159–169. https://doi.org/10.1093/genetics/165.1.159

Bonello, T.T., K.Z. Perez-Vale, K.D. Sumigray, and M. Peifer. 2018. Rap1 acts via multiple mechanisms to position Canoe and adherens junctions and mediate apical-basal polarity establishment. *Development*. 145: dev157941. https://doi.org/10.1242/dev.157941

Borghi, N., M. Sorokina, O.G. Shcherbakova, W.I. Weis, B.L. Pruitt, W.J. Nelson, and A.R. Dunn. 2012. E-cadherin is under constitutive actomyosin-generated tension that is increased at cell-cell contacts upon externally applied stretch. *Proc. Natl. Acad. Sci. USA*. 109: 12568–12573. https://doi.org/10.1073/pnas.1204390109

Boutillon, A., S. Escot, A. Elouin, D. Jahn, S. González-Tirado, J. Starruß, L. Brusch, and N.B. David. 2022. Guidance by followers ensures long-range coordination of cell migration through α-catenin mechanoperception. *Dev. Cell*. 57:1529–1544.e5. https://doi.org/10.1016/j.devcel.2022.05.001

Buckley, C.D., J. Tan, K.L. Anderson, D. Hanein, N. Volkmann, W.I. Weis, W.J. Nelson, and A.R. Dunn. 2014. Cell adhesion. The minimal cadherin-catenin complex binds to actin filaments under force. *Science*. 346: 1254211. https://doi.org/10.1126/science.1254211

Bush, M., B.M. Alhanshali, S. Qian, C.B. Stanley, W.T. Heller, T. Matsui, T.M. Weiss, I.D. Nicholl, T. Walz, D.J.E. Callaway, and Z. Bu. 2019. An ensemble of flexible conformations underlies mechanotransduction by the cadherin-catenin adhesion complex. *Proc. Natl. Acad. Sci. USA*. 116: 21545–21555. https://doi.org/10.1073/pnas.1911489116

Cavey, M., M. Rauzi, P.F. Lenne, and T. Lecuit. 2008. A two-tiered mechanism for stabilization and immobilization of E-cadherin. *Nature*. 453: 751–756. https://doi.org/10.1038/nature06953

Charras, G., and A.S. Yap. 2018. Tensile forces and mechanotransduction at cell-cell junctions. *Curr. Biol.* 28:R445–R457. https://doi.org/10.1016/j.cub.2018.02.003

Choi, W., K.C. Jung, K.S. Nelson, M.A. Bhat, G.J. Beitel, M. Peifer, and A.S. Fanning. 2011. The single Drosophila ZO-1 protein Polychaetoid regulates embryonic morphogenesis in coordination with Canoe/afadin and Enabled. *Mol. Biol. Cell*. 22:2010–2030. https://doi.org/10.1091/mbc.E10-12-1014

Choi, H.J., S. Pokutta, G.W. Cadwell, A.A. Bobkov, L.A. Bankston, R.C. Liddington, and W.I. Weis. 2012. αE-catenin is an autoinhibited molecule that coactivates vinculin. *Proc. Natl. Acad. Sci. USA*. 109:8576–8581. https://doi.org/10.1073/pnas.1203906109

Clarke, D.N., and A.C. Martin. 2021. Actin-based force generation and cell adhesion in tissue morphogenesis. *Curr. Biol.* 31:R667–R680. https://doi.org/10.1016/j.cub.2021.03.031

Costa, M., W. Raich, C. Agbunag, B. Leung, J. Hardin, and J.R. Priess. 1998. A putative catenin-cadherin system mediates morphogenesis of the Caenorhabditis elegans embryo. *J. Cell Biol.* 141:297–308. https://doi.org/10.1083/jcb.141.1.297

Cox, R.T., C. Kirkpatrick, and M. Peifer. 1996. Armadillo is required for adherens junction assembly, cell polarity, and morphogenesis during Drosophila embryogenesis. *J. Cell Biol.* 134:133–148. https://doi.org/10.1083/jcb.134.1.133

Desai, R., R. Sarpal, N. Ishiyama, M. Pellikka, M. Ikura, and U. Tepass. 2013. Monomeric α-catenin links cadherin to the actin cytoskeleton. *Nat. Cell Biol.* 15:261–273. https://doi.org/10.1038/ncb2685

Eritano, A.S., C.L. Bromley, A. Bolea Albero, L. Schütz, F.L. Wen, M. Takeda, T. Fukaya, M.M. Sami, T. Shibata, S. Lemke, and Y.C. Wang. 2020. Tissue-scale mechanical coupling reduces morphogenetic noise to ensure precision during epithelial folding. *Dev. Cell*. 53:212–228.e12. https://doi.org/10.1016/j.devcel.2020.02.012

Escobar, D.J., R. Desai, N. Ishiyama, S.S. Folmsbee, M.N. Novak, A.S. Flozak, R.L. Daugherty, R. Mo, D. Nanavati, R. Sarpal, et al. 2015. α-Catenin phosphorylation promotes intercellular adhesion through a dual-kinase mechanism. *J. Cell Sci.* 128:1150–1165. https://doi.org/10.1242/jcs.163824

Fernandez-Gonzalez, R., and J.A. Zallen. 2011. Oscillatory behaviors and hierarchical assembly of contractile structures in intercalating cells. *Phys. Biol.* 8:045005. https://doi.org/10.1088/1478-3975/8/4/045005

Fernandez-Gonzalez, R., S.d. M. Simoes, J.C. Röper, S. Eaton, and J.A. Zallen. 2009. Myosin II dynamics are regulated by tension in intercalating cells. *Dev. Cell*. 17:736–743. https://doi.org/10.1016/j.devcel.2009.09.003

Fernandez-Gonzalez, R., N. Balaghi, K. Wang, R. Hawkins, K. Rothenberg, C. McFaul, C. Schimmer, M. Ly, A. do Carmo, G. Scepanovic, et al. 2021. PyJAMAS: Open-source, multimodal segmentation and analysis of microscopy images. *Bioinformatics*. 38:594–596. https://doi.org/10.1093/bioinformatics/btab589

Foe, V.E. 1989. Mitotic domains reveal early commitment of cells in Drosophila embryos. *Development*. 107:1–22. https://doi.org/10.1242/dev.107.1.1

Häcker, U., and N. Perrimon. 1998. DRhoGEF2 encodes a member of the Dbl family of oncogenes and controls cell shape changes during gastrulation in Drosophila. *Genes Dev*. 12:274–284. https://doi.org/10.1101/gad.12.2.274

Han, M.K.L., E. Hoijman, E. Nöel, L. Garric, J. Bakkers, and J. de Rooij. 2016. αE-catenin-dependent mechanotransduction is essential for proper convergent extension in zebrafish. *Biol. Open*. 5:1461–1472. https://doi.org/10.1242/bio.021378

Han, M.K.L., G.N.M. van der Krogt, and J. de Rooij. 2017. Zygotic vinculin is not essential for embryonic development in zebrafish. *PLoS One*. 12: e0182278. https://doi.org/10.1371/journal.pone.0182278

Hara, Y., M. Shagirov, and Y. Toyama. 2016. Cell boundary elongation by non-autonomous contractility in cell oscillation. *Curr. Biol.* 26:2388–2396. https://doi.org/10.1016/j.cub.2016.07.003

Higashi, T., and A.L. Miller. 2017. Tricellular junctions: How to build junctions at the TRICkiest points of epithelial cells. *Mol. Biol. Cell*. 28: 2023–2034. https://doi.org/10.1091/mbc.E16-10-0697

Huang, J., W. Zhou, W. Dong, A.M. Watson, and Y. Hong. 2009. From the Cover: Directed, efficient, and versatile modifications of the Drosophila genome by genomic engineering. *Proc. Natl. Acad. Sci. USA*. 106: 8284–8289. https://doi.org/10.1073/pnas.0900641106

Huveneers, S., J. Oldenburg, E. Spanjaard, G. van der Krogt, I. Grigoriev, A. Akhmanova, H. Rehmann, and J. de Rooij. 2012. Vinculin associates with endothelial VE-cadherin junctions to control force-dependent remodeling. *J. Cell Biol*. 196:641–652. https://doi.org/10.1083/jcb.201108120

Ishiyama, N., and M. Ikura. 2012. The three-dimensional structure of the cadherin–catenin complex. In Adherens Junctions: From Molecular Mechanisms to Tissue Development and Disease. Springer: Berlin. 39–62. https://doi.org/10.1007/978-94-007-4186-7_3

Ishiyama, N., N. Tanaka, K. Abe, Y.J. Yang, Y.M. Abbas, M. Umitsu, B. Nagar, S.A. Bueler, J.L. Rubinstein, M. Takeichi, and M. Ikura. 2013. An autoinhibited structure of α-catenin and its implications for vinculin recruitment to adherens junctions. *J. Biol. Chem.* 288:15913–15925. https://doi.org/10.1074/jbc.M113.453928

Ishiyama, N., R. Sarpal, M.N. Wood, S.K. Barrick, T. Nishikawa, H. Hayashi, A.B. Kobb, A.S. Flozak, A. Yemelyanov, R. Fernandez-Gonzalez, et al. 2018. Force-dependent allostery of the α-catenin actin-binding domain controls adherens junction dynamics and functions. *Nat. Commun.* 9: 5121. https://doi.org/10.1038/s41467-018-07481-7

Jurado, J., J. de Navascués, and N. Gorfinkiel. 2016. α-Catenin stabilises Cadherin–Catenin complexes and modulates actomyosin dynamics to allow pulsatile apical contraction. *J. Cell Sci.* 129:4496–4508. https://doi.org/10.1242/jcs.193268

Jürgens, G., E. Wieschaus, C. Nüsslein-Volhard, and H. Kluding. 1984. Mutations affecting the pattern of the larval cuticle in Drosophila melanogaster. *Rouxs Arch. Dev. Biol.* 193:283–295. https://doi.org/10.1007/BF00848157

Kale, G.R., X. Yang, J.M. Philippe, M. Mani, P.F. Lenne, and T. Lecuit. 2018. Distinct contributions of tensile and shear stress on E-cadherin levels during morphogenesis. *Nat. Commun.* 9:5021. https://doi.org/10.1038/s41467-018-07448-8

Kim, T.J., S. Zheng, J. Sun, I. Muhamed, J. Wu, L. Lei, X. Kong, D.E. Leckband, and Y. Wang. 2015. Dynamic visualization of α-catenin reveals rapid, reversible conformation switching between tension states. *Curr. Biol.* 25:218–224. https://doi.org/10.1016/j.cub.2014.11.017

Klapholz, B., S.L. Herbert, J. Wellmann, R. Johnson, M. Parsons, and N.H. Brown. 2015. Alternative mechanisms for talin to mediate integrin function. *Curr. Biol.* 25:847–857. https://doi.org/10.1016/j.cub.2015.01.043

Kofron, M., A. Spagnuolo, M. Klymkowsky, C. Wylie, and J. Heasman. 1997. The roles of maternal alpha-catenin and plakoglobin in the early Xenopus embryo. *Development*. 124:1553–1560. https://doi.org/10.1242/dev.124.8.1553

Ladoux, B., W.J. Nelson, J. Yan, and R.M. Mège. 2015. The mechanotransduction machinery at work at adherens junctions. *Integr. Biol.* 7:1109–1119. https://doi.org/10.1039/c5ib00070j

le Duc, Q., Q. Shi, I. Blonk, A. Sonnenberg, N. Wang, D. Leckband, and J. de Rooij. 2010. Vinculin potentiates E-cadherin mechanosensing and is recruited to actin-anchored sites within adherens junctions in a myosin II-dependent manner. *J. Cell Biol.* 189:1107–1115. https://doi.org/10.1083/jcb.201001149

Le, S., M. Yu, S. Martin, J. Hardin, and J. Yan. 2021. Mechano-Biochemical Regulation of the C. elegans HMP1-HMP2 protein complex. *bioRxiv*. (Preprint posted September 28, 2021). https://doi.org/10.1101/2021.09.27.462086

Leckband, D.E., and J. de Rooij. 2014. Cadherin adhesion and mechanotransduction. *Annu. Rev. Cell Dev. Biol.* 30:291–315. https://doi.org/10.1146/annurev-cellbio-100913-013212

Lecuit, T., and A.S. Yap. 2015. E-cadherin junctions as active mechanical integrators in tissue dynamics. *Nat. Cell Biol.* 17:533–539. https://doi.org/10.1038/ncb3136

Levayer, R., and T. Lecuit. 2013. Oscillation and polarity of E-cadherin asymmetries control actomyosin flow patterns during morphogenesis. *Dev. Cell*. 26:162–175. https://doi.org/10.1016/j.devcel.2013.06.020

Li, J., J. Newhall, N. Ishiyama, C. Gottardi, M. Ikura, D.E. Leckband, and E. Tajkhorshid. 2015. Structural determinants of the mechanical stability of α-catenin. *J. Biol. Chem.* 290:18890–18903. https://doi.org/10.1074/jbc.M115.647941

Lin, C., J. Xu, W. Yang, C. Wang, Y. Li, L. Cheng, L. Zhang, and J. Hsu. 2017. Smurf downregulates echinoid in the amnioserosa to regulate Drosophila dorsal closure. *Genetics*. 206:985–992. https://doi.org/10.1534/genetics.116.196527

Lowe, N., J.S. Rees, J. Roote, E. Ryder, I.M. Armean, G. Johnson, E. Drummond, H. Spriggs, J. Drummond, J.P. Magbanua, and UK Drosophila Protein Trap Screening Consortium. 2014. Analysis of the expression patterns, subcellular localisations and interaction partners of Drosophila proteins using a pigP protein trap library. *Development*. 141:3994–4005. https://doi.org/10.1242/dev.111054

Lye, C.M., H.W. Naylor, and B. Sanson. 2014. Subcellular localisations of the CPTI collection of YFP-tagged proteins in Drosophila embryos. *Development*. 141:4006–4017. https://doi.org/10.1242/dev.111310

Maartens, A.P., J. Wellmann, E. Wictome, B. Klapholz, H. Green, and N.H. Brown. 2016. Drosophila vinculin is more harmful when hyperactive than absent, and can circumvent integrin to form adhesion complexes. *J. Cell Sci.* 129:4354–4365. https://doi.org/10.1242/jcs.189878

Maki, K., S.W. Han, Y. Hirano, S. Yonemura, T. Hakoshima, and T. Adachi. 2016. Mechano-adaptive sensory mechanism of α-catenin under tension. *Sci. Rep.* 6:24878. https://doi.org/10.1038/srep24878

Manning, L.A., K.Z. Perez-Vale, K.N. Schaefer, M.T. Sewell, and M. Peifer. 2019. The Drosophila Afadin and ZO-1 homologues Canoe and Polychaetoid act in parallel to maintain epithelial integrity when challenged by adherens junction remodeling. *Mol. Biol. Cell*. 30:1938–1960. https://doi.org/10.1091/mbc.E19-04-0209

Marie, H., S.J. Pratt, M. Betson, H. Epple, J.T. Kittler, L. Meek, S.J. Moss, S. Troyanovsky, D. Attwell, G.D. Longmore, and V.M. Braga. 2003. The LIM protein Ajuba is recruited to cadherin-dependent cell junctions through an association with α-catenin. *J. Biol. Chem.* 278:1220–1228. https://doi.org/10.1074/jbc.M205391200

Martin, A.C. 2020. The physical mechanisms of Drosophila gastrulation: Mesoderm and endoderm invagination. *Genetics*. 214:543–560. https://doi.org/10.1534/genetics.119.301292

Martin, A.C., M. Gelbart, R. Fernandez-Gonzalez, M. Kaschube, and E.F. Wieschaus. 2010. Integration of contractile forces during tissue invagination. *J. Cell Biol.* 188:735–749. https://doi.org/10.1083/jcb.200910099

Martino, F., A.R. Perestrelo, V. Vinarský, S. Pagliari, and G. Forte. 2018. Cellular mechanotransduction: From tension to function. *Front. Physiol.* 9:824. https://doi.org/10.3389/fphys.2018.00824

Matsuzawa, K., T. Himoto, Y. Mochizuki, and J. Ikenouchi. 2018. α-Catenin controls the anisotropy of force distribution at Cell-Cell junctions during collective cell migration. *Cell Rep.* 23:3447–3456. https://doi.org/10.1016/j.celrep.2018.05.070

Mège, R.M., and N. Ishiyama. 2017. Integration of cadherin adhesion and cytoskeleton at adherens junctions. *Cold Spring Harbor Perspect. Biol.* 9:a028738. https://doi.org/10.1101/cshperspect.a028738

Miller, K.G., C.M. Field, and B.M. Alberts. 1989. Actin-binding proteins from Drosophila embryos: A complex network of interacting proteins detected by F-actin affinity chromatography. *J. Cell Biol.* 109:2963–2975. https://doi.org/10.1083/jcb.109.6.2963

Munjal, A., J.M. Philippe, E. Munro, and T. Lecuit. 2015. A self-organized biomechanical network drives shape changes during tissue morphogenesis. *Nature*. 524:351–355. https://doi.org/10.1038/nature14603

Nathaniel Clarke, D., C.J. Lowe, and W. James Nelson. 2019. The cadherin-catenin complex is necessary for cell adhesion and embryogenesis in Nematostella vectensis. *Dev. Biol.* 447:170–181. https://doi.org/10.1016/j.ydbio.2019.01.007

Nieset, J.E., A.R. Redfield, F. Jin, K.A. Knudsen, K.R. Johnson, and M.J. Wheelock. 1997. Characterization of the interactions of alpha-catenin with alpha-actinin and beta-catenin/plakoglobin. *J. Cell Sci.* 110:1013–1022. https://doi.org/10.1242/jcs.110.8.1013

Paré, A.C., and J.A. Zallen. 2020. Cellular, molecular, and biophysical control of epithelial cell intercalation. *Curr. Top. Dev. Biol.* 136:167–193. https://doi.org/10.1016/bs.ctdb.2019.11.014

Perez-Vale, K.Z., K.D. Yow, R.I. Johnson, A.E. Byrnes, T.M. Finegan, K.C. Slep, and M. Peifer. 2021. Multivalent interactions make adherens junction-cytoskeletal linkage robust during morphogenesis. *J. Cell Biol.* 220:e202104087. https://doi.org/10.1083/jcb.202104087

Pinheiro, D., and Y. Bellaïche. 2018. Mechanical force-driven adherens junction remodeling and epithelial dynamics. *Dev. Cell*. 47:3–19. https://doi.org/10.1016/j.devcel.2018.09.014

Pokutta, S., F. Drees, Y. Takai, W.J. Nelson, and W.I. Weis. 2002. Biochemical and structural definition of the l-afadin- and actin-binding sites of α-catenin. *J. Biol. Chem.* 277:18868–18874. https://doi.org/10.1074/jbc.M201463200

Pratt, S.J., H. Epple, M. Ward, Y. Feng, V.M. Braga, and G.D. Longmore. 2005. The LIM protein Ajuba influences p130Cas localization and Rac1 activity during cell migration. *J. Cell Biol.* 168:813–824. https://doi.org/10.1083/jcb.200406083

Rangarajan, E.S., and T. Izard. 2012. The cytoskeletal protein α-catenin unfurls upon binding to vinculin. *J. Biol. Chem.* 287:18492–18499. https://doi.org/10.1074/jbc.M112.351023

Rauskolb, C., S. Sun, G. Sun, Y. Pan, and K.D. Irvine. 2014. Cytoskeletal tension inhibits Hippo signaling through an Ajuba-Warts complex. *Cell*. 158:143–156. https://doi.org/10.1016/j.cell.2014.05.035

Rauskolb, C., E. Cervantes, F. Madere, and K.D. Irvine. 2019. Organization and function of tension-dependent complexes at adherens junctions. *J. Cell Sci.* 132:jcs224063. https://doi.org/10.1242/jcs.224063

Rauzi, M., P.F. Lenne, and T. Lecuit. 2010. Planar polarized actomyosin contractile flows control epithelial junction remodelling. *Nature*. 468:1110–1114. https://doi.org/10.1038/nature09566

Razzell, W., M.E. Bustillo, and J.A. Zallen. 2018. The force-sensitive protein Ajuba regulates cell adhesion during epithelial morphogenesis. *J. Cell Biol.* 217:3715–3730. https://doi.org/10.1083/jcb.201801171

Rimm, D.L., E.R. Koslov, P. Kebriaei, C.D. Cianci, and J.S. Morrow. 1995. Alpha 1(E)-catenin is an actin-binding and -bundling protein mediating the attachment of F-actin to the membrane adhesion complex. *Proc. Natl. Acad. Sci. USA*. 92:8813–8817. https://doi.org/10.1073/pnas.92.19.8813

Rothenberg, K.E., and R. Fernandez-Gonzalez. 2019. Forceful closure: Cytoskeletal networks in embryonic wound repair. *Mol. Biol. Cell*. 30:1353–1358. https://doi.org/10.1091/mbc.E18-04-0248

Sabino, D., N.H. Brown, and R. Basto. 2011. Drosophila Ajuba is not an Aurora-A activator but is required to maintain Aurora-A at the centrosome. *J. Cell Sci.* 124:1156–1166. https://doi.org/10.1242/jcs.076711

Sakakibara, S., K. Mizutani, A. Sugiura, A. Sakane, T. Sasaki, S. Yonemura, and Y. Takai. 2020. Afadin regulates actomyosin organization through αE-catenin at adherens junctions. *J. Cell Biol.* 219:e201907079. https://doi.org/10.1083/jcb.201907079

Sarpal, R., M. Pellikka, R.R. Patel, F.Y.W. Hui, D. Godt, and U. Tepass. 2012. Mutational analysis supports a core role for Drosophila α-catenin in adherens junction function. *J. Cell Sci.* 125:233–245. https://doi.org/10.1242/jcs.096644

Sarpal, R., V. Yan, L. Kazakova, L. Sheppard, J.C. Yu, R. Fernandez-Gonzalez, and U. Tepass. 2019. Role of α-Catenin and its mechanosensing properties in regulating Hippo/YAP-dependent tissue growth. *PLoS Genet.* 15:e1008454. https://doi.org/10.1371/journal.pgen.1008454

Sawyer, J.K., N.J. Harris, K.C. Slep, U. Gaul, and M. Peifer. 2009. The Drosophila afadin homologue Canoe regulates linkage of the actin cytoskeleton to adherens junctions during apical constriction. *J. Cell Biol.* 186:57–73. https://doi.org/10.1083/jcb.200904001

Sawyer, J.K., W. Choi, K.C. Jung, L. He, N.J. Harris, and M. Peifer. 2011. A contractile actomyosin network linked to adherens junctions by Canoe/afadin helps drive convergent extension. *Mol. Biol. Cell*. 22:2491–2508. https://doi.org/10.1091/mbc.E11-05-0411

Schepis, A., D. Sepich, and W.J. Nelson. 2012. αE-catenin regulates cell-cell adhesion and membrane blebbing during zebrafish epiboly. *Development*. 139:537–546. https://doi.org/10.1242/dev.073932

Schindelin, J., I. Arganda-Carreras, E. Frise, V. Kaynig, M. Longair, T. Pietzsch, S. Preibisch, C. Rueden, S. Saalfeld, B. Schmid, et al. 2012. Fiji: An open-source platform for biological-image analysis. *Nat. Met.* 9: 676–682. https://doi.org/10.1038/nmeth.2019

Seddiki, R., G.H.N.S. Narayana, P.O. Strale, H.E. Balcioglu, G. Peyret, M. Yao, A.P. Le, C. Teck Lim, J. Yan, B. Ladoux, and R.M. Mège. 2018. Force-dependent binding of vinculin to α-catenin regulates cell-cell contact stability and collective cell behavior. *Mol. Biol. Cell*. 29:380–388. https://doi.org/10.1091/mbc.E17-04-0231

Serre, J.M., B. Lucas, S.C.T. Martin, J.A. Heier, X. Shao, and J. Hardin. 2022. C. elegans srGAP is an α-catenin M domain-binding protein that strengthens cadherin-dependent adhesion during morphogenesis. *Development*. 149:dev200775. https://doi.org/10.1242/dev.200775

Simões, S., Y. Oh, M.F.Z. Wang, R. Fernandez-Gonzalez, and U. Tepass. 2017. Myosin II promotes the anisotropic loss of the apical domain during Drosophila neuroblast ingression. *J. Cell Biol.* 216:1387–1404. https://doi.org/10.1083/jcb.201608038

Stephenson, R.E., T. Higashi, I.S. Erofeev, T.R. Arnold, M. Leda, A.B. Goryachev, and A.L. Miller. 2019. Rho flares repair local tight junction leaks. *Dev. Cell*. 48:445–459.e5. https://doi.org/10.1016/j.devcel.2019.01.016

Takahashi, K., T. Matsuo, T. Katsube, R. Ueda, and D. Yamamoto. 1998. Direct binding between two PDZ domain proteins Canoe and ZO-1 and their roles in regulation of the jun N-terminal kinase pathway in Drosophila morphogenesis. *Mech. Dev.* 78:97–111. https://doi.org/10.1016/s0925-4773(98)00151-8

Tepass, U., E. Gruszynski-DeFeo, T.A. Haag, L. Omatyar, T. Török, and V. Hartenstein. 1996. Shotgun encodes Drosophila E-cadherin and is preferentially required during cell rearrangement in the neurectoderm and other morphogenetically active epithelia. *Genes Dev.* 10:672–685. https://doi.org/10.1101/gad.10.6.672

Terekhova, K., S. Pokutta, Y.S. Kee, J. Li, E. Tajkhorshid, G. Fuller, A.R. Dunn, and W.I. Weis. 2019. Binding partner- and force-promoted changes in αE-catenin conformation probed by native cysteine labeling. *Sci. Rep.* 9: 15375. https://doi.org/10.1038/s41598-019-51816-3

Tetley, R.J., G.B. Blanchard, A.G. Fletcher, R.J. Adams, and B. Sanson. 2016. Unipolar distributions of junctional Myosin II identify cell stripe boundaries that drive cell intercalation throughout Drosophila axis extension. *Elife*. 5:e12094. https://doi.org/10.7554/eLife.12094

Thomas, W.A., C. Boscher, Y.S. Chu, D. Cuvelier, C. Martinez-Rico, R. Seddiki, J. Heysch, B. Ladoux, J.P. Thiery, R.M. Mege, and S. Dufour. 2013. α-Catenin and vinculin cooperate to promote high E-cadherin-based adhesion strength. *J. Biol. Chem.* 288:4957–4969. https://doi.org/10.1074/jbc.M112.403774

Torres, M., A. Stoykova, O. Huber, K. Chowdhury, P. Bonaldo, A. Mansouri, S. Butz, R. Kemler, and P. Gruss. 1997. An α-E-catenin gene trap mutation defines its function in preimplantation development. *Proc. Natl. Acad. Sci. USA*. 94:901–906. https://doi.org/10.1073/pnas.94.3.901

Trichas, G., A.M. Smith, N. White, V. Wilkins, T. Watanabe, A. Moore, B. Joyce, J. Sugnaseelan, T.A. Rodriguez, D. Kay, et al. 2012. Multi-cellular rosettes in the mouse visceral endoderm facilitate the ordered migration of anterior visceral endoderm cells. *PLoS Biol.* 10:e1001256. https://doi.org/10.1371/journal.pbio.1001256

Twiss, F., Q. le Duc, S. Van Der Horst, H. Tabdili, G. Van Der Krogt, N. Wang, H. Rehmann, S. Huveneers, D.E. Leckband, and J. De Rooij. 2012. Vinculin-dependent Cadherin mechanosensing regulates efficient epithelial barrier formation. *Biol. Open*. 1:1128–1140. https://doi.org/10.1242/bio.20122428

Vanderleest, T.E., C.M. Smits, Y. Xie, C.E. Jewett, J.T. Blankenship, and D. Loerke. 2018. Vertex sliding drives intercalation by radial coupling of adhesion and actomyosin networks during Drosophila germband extension. *Elife*. 7:e34586. https://doi.org/10.7554/eLife.34586

Wang, Y.C., Z. Khan, and E.F. Wieschaus. 2013. Distinct Rap1 activity states control the extent of epithelial invagination via α-catenin. *Dev. Cell*. 25: 299–309. https://doi.org/10.1016/j.devcel.2013.04.002

Wang, A., A.R. Dunn, and W.I. Weis. 2022. Mechanism of the cadherin-catenin F-actin catch bond interaction. *Elife*. 11:e80130. https://doi.org/10.7554/eLife.80130

Wei, S.Y., L.M. Escudero, F. Yu, L.H. Chang, L.Y. Chen, Y.H. Ho, C.M. Lin, C.S. Chou, W. Chia, J. Modolell, and J.C. Hsu. 2005. Echinoid is a component of adherens junctions that cooperates with DE-Cadherin to mediate cell adhesion. *Dev. Cell*. 8:493–504. https://doi.org/10.1016/j.devcel.2005.03.015

Witzel, H.R., B. Jungblut, C.P. Choe, J.G. Crump, T. Braun, and G. Dobreva. 2012. The LIM protein Ajuba restricts the second heart field progenitor pool by regulating Isl1 activity. *Dev. Cell*. 23:58–70. https://doi.org/10.1016/j.devcel.2012.06.005

Xu, W., H. Baribault, and E.D. Adamson. 1998. Vinculin knockout results in heart and brain defects during embryonic development. *Development*. 125:327–337. https://doi.org/10.1242/dev.125.2.327

Xu, X.P., S. Pokutta, M. Torres, M.F. Swift, D. Hanein, N. Volkmann, and W.I. Weis. 2020. Structural basis of αE-catenin-F-actin catch bond behavior. *Elife*. 9:e60878. https://doi.org/10.7554/eLife.60878

Yao, M., W. Qiu, R. Liu, A.K. Efremov, P. Cong, R. Seddiki, M. Payre, C.T. Lim, B. Ladoux, R.M. Mège, and J. Yan. 2014. Force-dependent conformational switch of α-catenin controls vinculin binding. *Nat. Commun.* 5: 4525. https://doi.org/10.1038/ncomms5525

Yonemura, S., Y. Wada, T. Watanabe, A. Nagafuchi, and M. Shibata. 2010. alpha-Catenin as a tension transducer that induces adherens junction development. *Nat. Cell Biol.* 12:533–542. https://doi.org/10.1038/ncb2055

Yu, J.C., and R. Fernandez-Gonzalez. 2016. Local mechanical forces promote polarized junctional assembly and axis elongation in Drosophila. *Elife*. 5: e10757. https://doi.org/10.7554/eLife.10757

Yu, H.H., and J.A. Zallen. 2020. Abl and Canoe/Afadin mediate mechanotransduction at tricellular junctions. *Science*. 370:eaba5528. https://doi.org/10.1126/science.aba5528

Zallen, J.A., and J.T. Blankenship. 2008. Multicellular dynamics during epithelial elongation. *Semin. Cell Dev. Biol.* 19:263–270. https://doi.org/10.1016/j.semcdb.2008.01.005

Zallen, J.A., and E. Wieschaus. 2004. Patterned gene expression directs bipolar planar polarity in Drosophila. *Dev. Cell*. 6:343–355. https://doi.org/10.1016/s1534-5807(04)00060-7

Zirin, J., Y. Hu, L. Liu, D. Yang-Zhou, R. Colbeth, D. Yan, B. Ewen-Campen, R. Tao, E. Vogt, S. VanNest, et al. 2020. Large-scale transgenic Drosophila resource collections for loss-and gain-of-function studies. *Genetics*. 214: 755–767. https://doi.org/10.1534/genetics.119.302964

Supplemental material

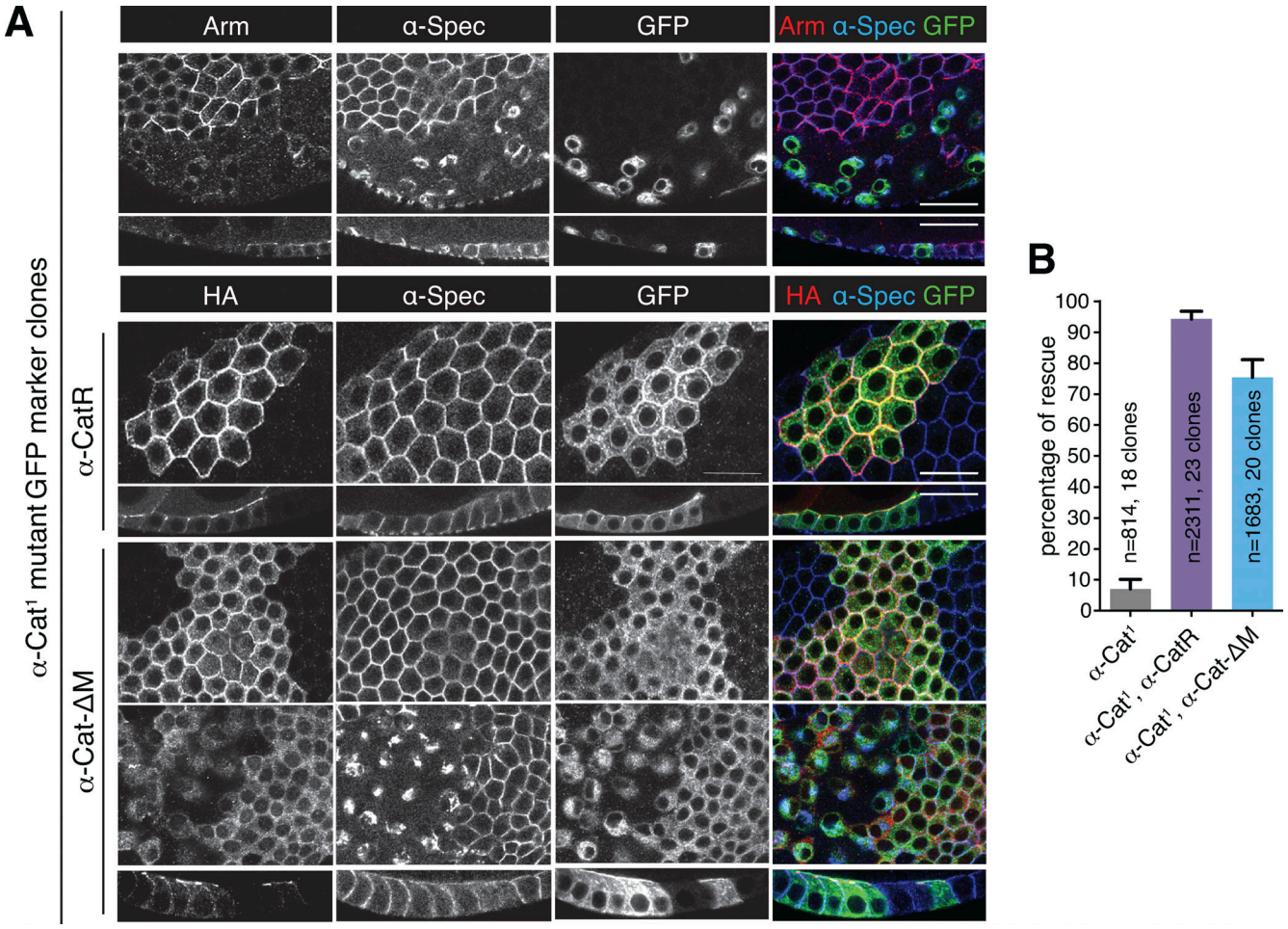

Figure S1. **Most follicular epithelia are normal when the M region is deleted. (A)** Follicular epithelium clones positively marked with GFP in indicated genotypes. α-Cat null mutant cells show strongly reduced levels of Arm and display cytoplasmic aggregates of α-Spectrin. Expression of α-CatR and α-Cat-ΔM in α-Cat mutant cells substantially rescue these defects. Scale bar, 20 µm. **(B)** Comparison of rescue activities of α-CatR and α-Cat-ΔM when expressed in α-Cat mutant cells in the follicular epithelium. Data are presented as mean ± SEM, *n* = number of cells analyzed, pooled from a number of clones.

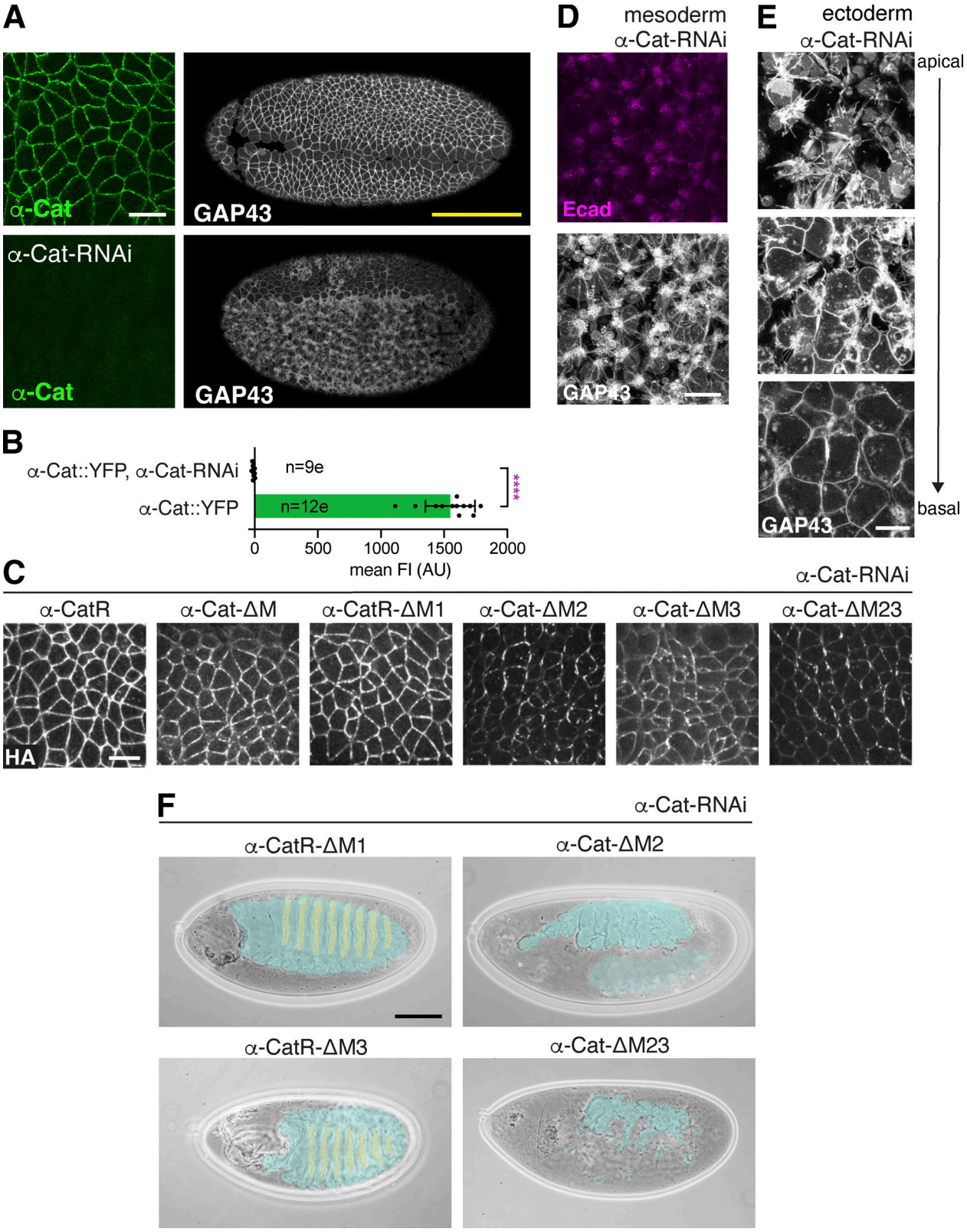

Figure S2. **α-*Cat-RNAi* knockdown and distribution and activity of M region deletion constructs. (A)** α-*Cat-RNAi* expressed by mat-GAL4 causes loss of any detectable cortical α-Cat in stage 8 embryos. Yellow scale bar, 100 µm; white scale bars, 10 µm. **(B)** Quantification of average levels of cortical α-Cat per embryo. Significance calculated by Mann-Whitney two-tailed *t* test, **** = P < 0.0001. Bar height, mean; error bars, SD; *n* = number of embryos (e). **(C)** Immunostaining and localization of HA-tagged α-Cat constructs expressed in embryos with α-*Cat-RNAi* background. Scale bar, 10 µm. **(D and E)** Close-ups of the mesoderm (C) and lateral ectoderm (D) of α-*Cat-RNAi* expressing embryos, showing membrane tethers and loss of AJs. Cells lose contact apically while basal membranes remain in contact. Scale bar, 10 µm. **(F)** Example images of terminal cuticle phenotypes of α-*Cat-RNAi α-CatX* embryos. Scale bar, 100 µm.

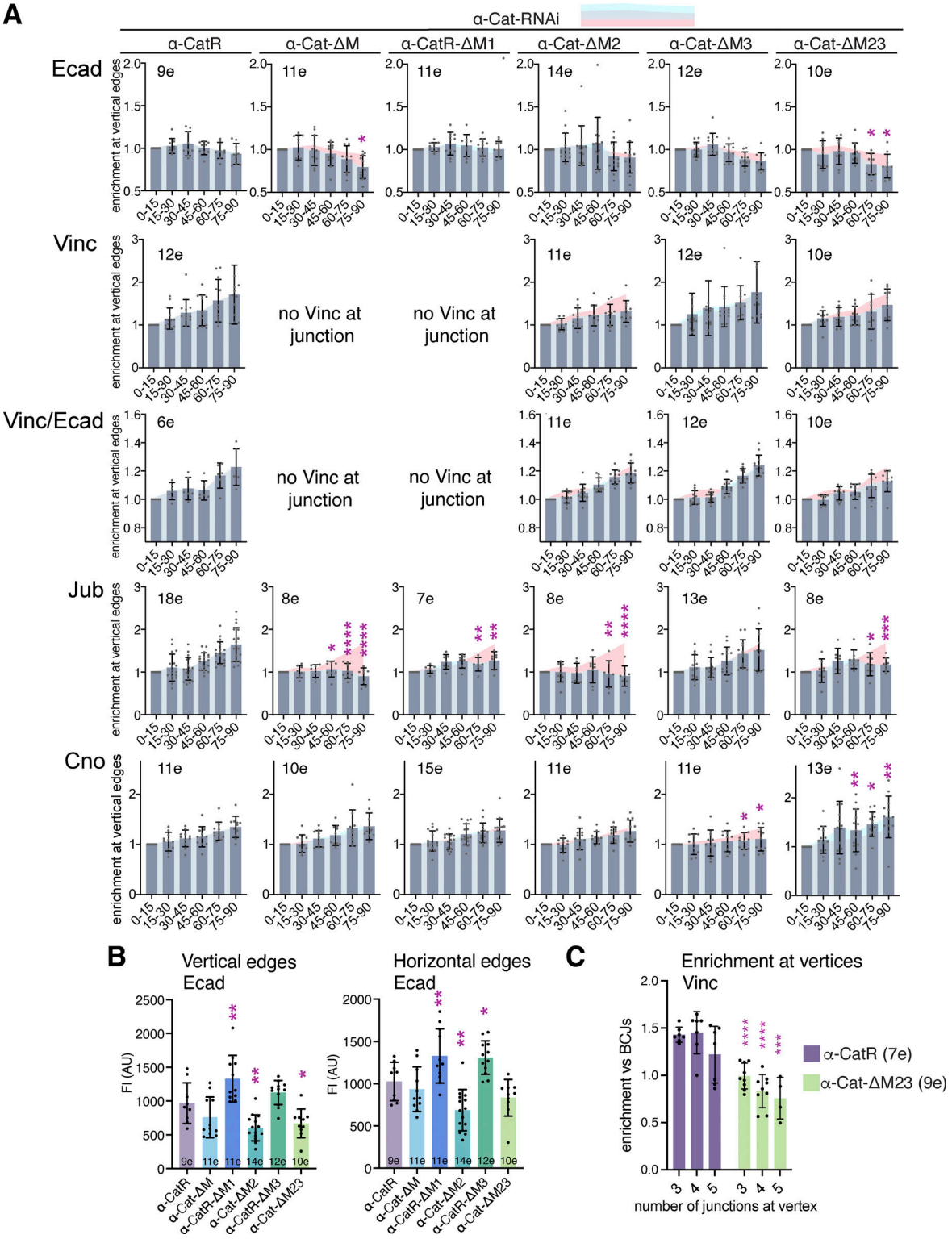

Figure S3. **Planar polarity analysis of AJ proteins in embryos expressing M region deletion constructs in an α-*Cat-RNAi* background**. **(A)** Plots of the fold changes of the average FI of edges within 15° bins versus that of the 0–15°bin (representing horizontal edges, 0° = anterior–posterior axis). Each dot represents the ratio derived from one embryo. Transparent pink and cyan shapes reflect control and experimental means, respectively, drawn to the height of each bar for ease of comparison. Where overlapping, gray is seen where experimental mean is reduced compared to control pink is visible, and conversely where increased cyan is visible. Significance calculated by ordinary two-way ANOVA with uncorrected Fisher's LSD for conditions within the same row. **(B)** Graphs show the mean junctional fluorescent signal per embryo of Ecad along edges in the horizontal or vertical bins in α-*Cat-RNAi α-CatX* embryos. Significance given by ordinary one-way ANOVA with uncorrected Fisher's LSD. **(C)** Enrichment of Vinc FI at vertices linked by three, four, or five junctions per α-*Cat-RNAi α-CatX* embryos. Significance given by ordinary two-way ANOVA with Tukey's multiple comparison test. For A–C, *n* = number of embryos analyzed (e), bar height represents mean, error bars show SD, **** = P < 0.0001, *** = P < 0.001, ** = P < 0.01, * = P < 0.05.

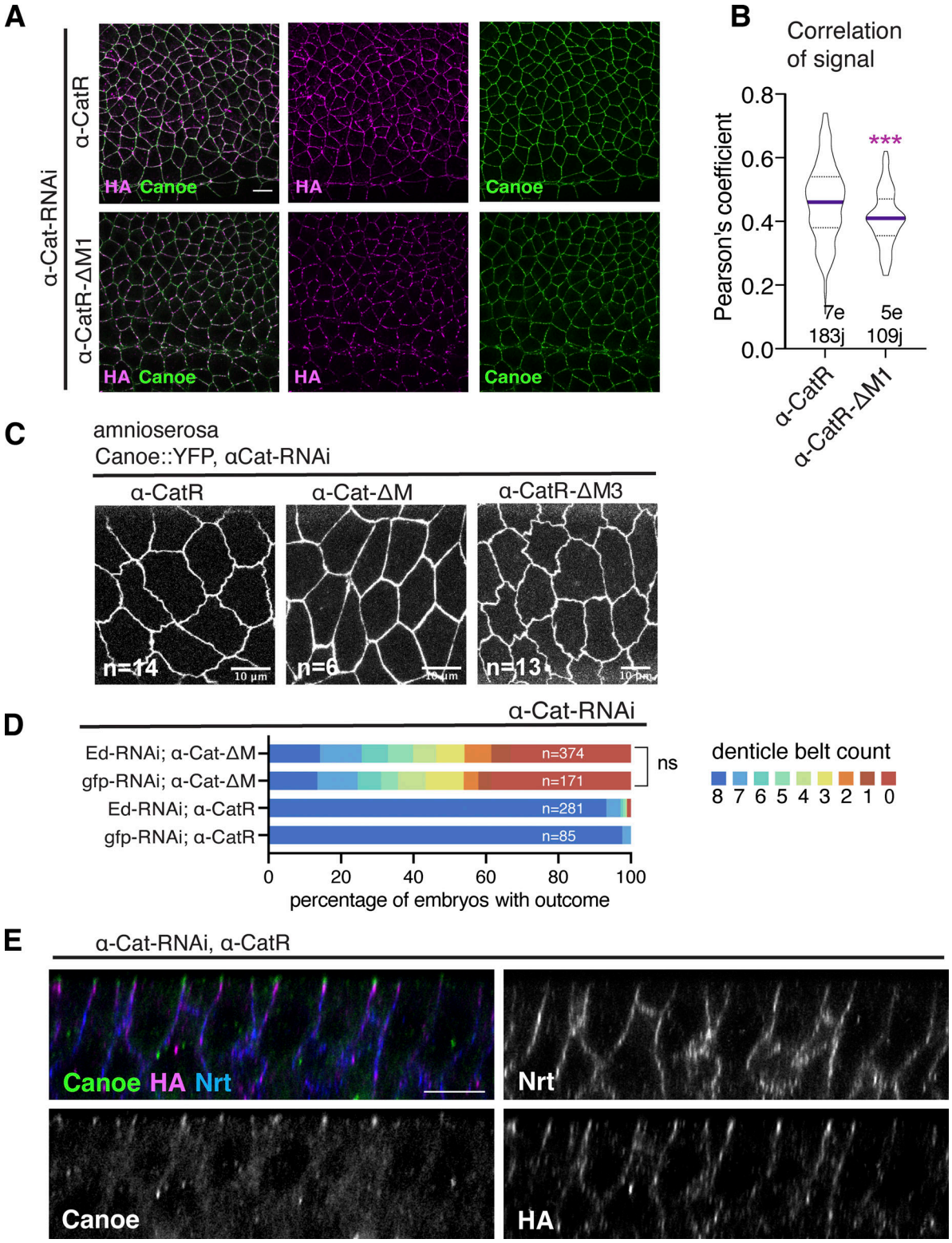

Figure S4. **Cno recruitment to AJs is largely α-Cat-independent. (A)** Examples of gastrulating α-*Cat-RNAi α-CatX* embryos heat-fixed and immunostained for α-CatR or α-CatR-ΔM1 (HA-tagged) and Cno. α-CatR-ΔM1 rescued embryos show a more irregular distribution than α-CatR. Scale bar, 10 µm. **(B)** Quantification of the colocalization between Cno and α-Cat construct. Significance calculated by Mann-Whitney two-tailed *t* test (*** = P < 0.001). Bold line shows the median, dotted lines represent interquartile ranges, and *n* = a pooled number of junctions analyzed (j) from a number of embryos (e). **(C)** Live imaged examples of Cno::YFP signal in the amnioserosa of α-*Cat-RNAi α-CatX* embryos; *n* = number of embryos observed. Scale bar, 10 µm. **(D)** Ed-RNAi does not change adhesion phenotypes in α-*Cat-RNAi α-CatX* embryos. Quantification of intact denticle belts; *n* = number of embryos analyzed. *gfp-RNAi* controls same as in Fig. 5 E. **(E)** Cross-section of the lateral ectoderm of an α-*Cat-RNAi* α-*CatR* embryo at stage 8 showing that Cno signal is apical to the HA-tagged α-Cat construct.

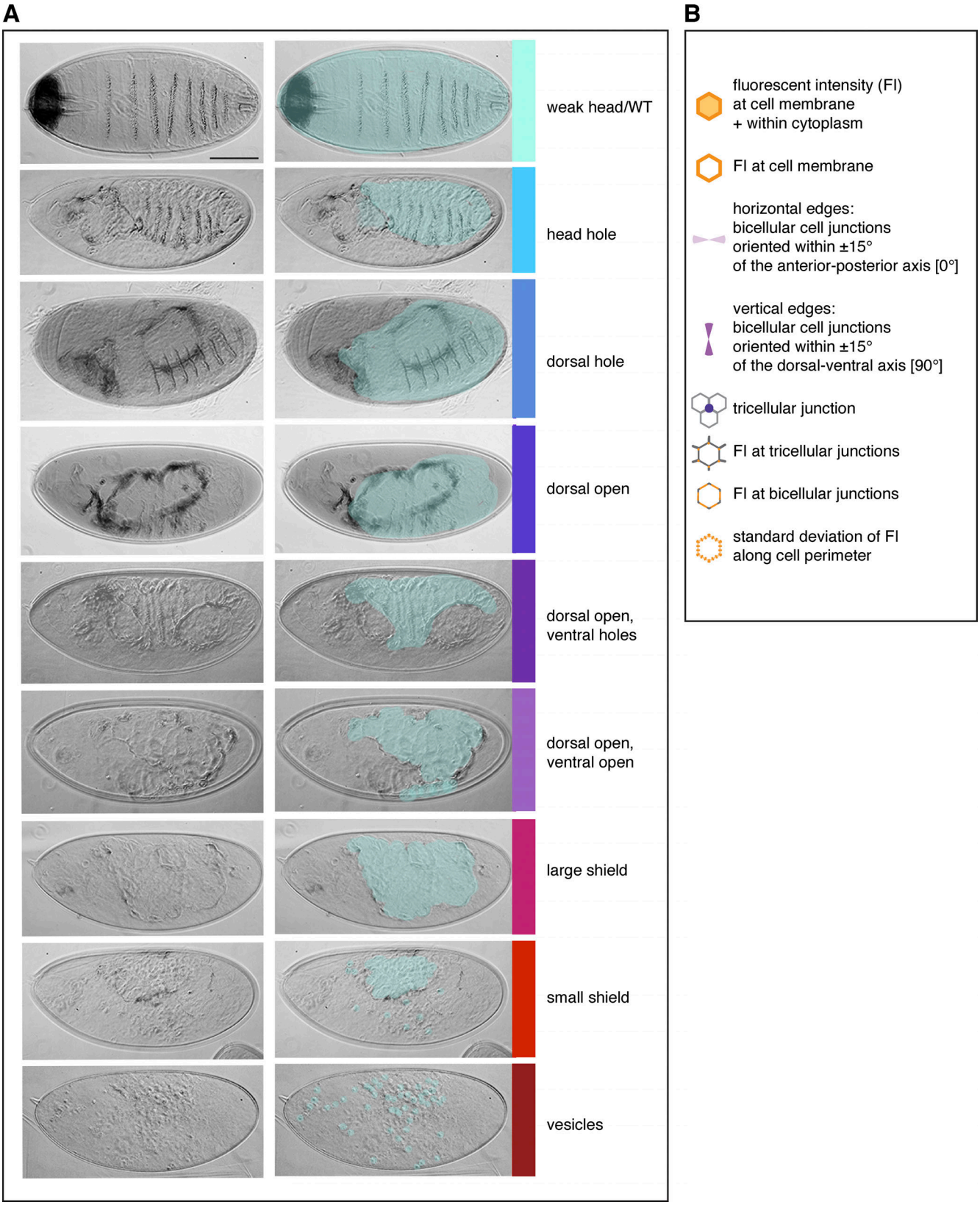

Figure S5. **Phenotypic categories of embryonic cuticle defects. (A)** Original images shown at left, overlays in cyan at right highlight regions of secreted cuticle. Color key at right corresponds to legend used in Fig. 9, A and B. Scale bar, 100 µm. **(B)** Legend for schematics that describe measurements plotted.

Video 1. **Failure of mesoderm invagination in embryo expressing α-Cat-RNAi.** Timestamp, min:s. Ecad::GFP, green; GAP43::mCherry, magenta. Images were taken every 30 s and displayed at 8 frames per second.

Video 2. **Gastrulation in an α-*Cat-RNAi α-CatR* embryo.** Timestamp, min:s. Ecad::GFP, green; GAP43::mCherry, magenta. Images were taken every 30 s and displayed at 8 frames per second.

Video 3. **Strong defects in an α-*Cat-RNAi α-Cat-ΔM* embryo.** Timestamp, min:s. Ecad::GFP, green; GAP43::mCherry, magenta. Images were taken every 30 s and displayed at 8 frames per second.

Video 4. **Moderate defects in an α-*Cat-RNAi α-Cat-ΔM* embryo.** Timestamp, min:s. Ecad::GFP, green; GAP43::mCherry, magenta. Images were taken every 30 s and displayed at 8 frames per second.

Video 5. **Gastrulation in an α-*Cat-RNAi α-CatR-ΔM1* embryo.** Timestamp, min:s. Ecad::GFP, green; GAP43::mCherry, magenta. Images were taken every 30 s and displayed at 8 frames per second.

Video 6. **Gastrulation in an α-*Cat-RNAi α-Cat-ΔM23* embryo.** Timestamp, min:s. Ecad::GFP, green; GAP43::mCherry, magenta. Images were taken every 30 s and displayed at 8 frames per second.

Video 7. **Example of an α-*Cat-RNAi α-CatR-ΔM3* embryo with stronger defects.** Timestamp, min:s. Ecad::GFP, green; GAP43::mCherry, magenta. Images were taken every 30 s and displayed at 8 frames per second.

Video 8. **Gastrulation in an α-*Cat-RNAi α-Cat-ΔM2* embryo.** Timestamp, min:s. Ecad::GFP, green; GAP43::mCherry, magenta. Images were taken every 30 s and displayed at 8 frames per second.

Video 9. **Laser ablation in germband cells expressing Jub::GFP and α-Cat-RNAi with α-CatR (at left) or α-Cat-ΔM (at right).** Timestamp, min:s. Images were taken every 10 s and displayed at 3 frames per second.

Video 10. **Laser ablation in germband cells expressing Cno::YFP and α-Cat-RNAi with α-CatR (at left) or α-Cat-ΔM (at right).** Timestamp, min:s. Images were taken every 10 s and displayed at 3 frames per second.

Provided online is Table S1, which contains a summary of genotypes used for each figure panel and breakpoints of constructs analyzed.